

# Realizing Quantum Wireless Sensing Without Extra Reference Sources: Architecture, Algorithm, and Sensitivity Maximization

Mingyao Cui, Qunsong Zeng, Zhanwei Wang, and Kaibin Huang, *Fellow, IEEE*

**Abstract**—Rydberg Atomic REceivers (RAREs) have shown compelling advantages in the precise measurement of radio-frequency signals, empowering quantum wireless sensing. Existing RARE-based sensing systems primarily rely on the heterodyne-sensing technique, which introduces an extra reference source to serve as the *atomic mixer*. However, this approach entails a bulky transceiver architecture and is limited in the supportable sensing bandwidth. To address these challenges, we propose self-heterodyne sensing, a novel concept where the self-interference caused by the transmitter acts as the reference signal. It is shown that a self-heterodyne RARE functions as an *atomic autocorrelator*, eliminating the need for extra reference sources while supporting sensing signals with much wider bandwidth than the conventional heterodyne-sensing method. Next, a two-stage algorithm is devised to estimate the target range for self-heterodyne RAREs. This algorithm is shown to closely approach the Cramér-Rao lower bound. Furthermore, we introduce the power-trajectory (*P*-trajectory) design for RAREs, which maximizes the sensing sensitivity through time-varying transmission power optimization. A heuristic *P*-trajectory is developed to capture the profile of the asymptotically optimal time-varying power. This design is then extended to practical *P*-trajectories by incorporating the transmitter power constraints. Numerical results validate the superiority of the proposed designs for quantum wireless sensing.

**Index Terms**—Rydberg atomic receivers, wireless communications, quantum sensing.

## I. INTRODUCTION

The precise measurement of radio-frequency (RF) signals is fundamental to the digital age, serving as a basic operation in wireless communication, remote sensing, e-health, and radar systems. Originating from the field of quantum sensing, Rydberg Atomic REceiver (RARE) has recently emerged as a new concept in high-precision wireless detection by harnessing the quantum properties of Rydberg atoms [1]–[3]. Specifically, Rydberg atoms are highly excited atoms in which one or more electrons have transitioned from their ground-state energy level to a higher energy state. Due to their large electric dipole moments, Rydberg atoms can strongly interact with incident RF signals, triggering electron transitions between resonant energy levels [3]. Capitalizing on these transitions, RAREs can capture the amplitude, frequency, phase, and polarization of RF signals with unparalleled precision. As a result, RAREs have the potential to work in tandem with or even replace traditional RF receivers, to empower next-generation wireless communication and sensing systems [4]–[8].

The advantages of RAREs include the extremely high sensitivity and wide range of detectable frequencies among others.

Specifically, the large electric dipole moments of Rydberg atoms can significantly amplify the incoming RF signals [9]. This achieves a sensitivity higher than that of their classical counterparts. Theoretical analysis based on the standard quantum limit (SQL) predicts a sensitivity limit for RAREs on the order of  $10 \text{ pV/cm}/\sqrt{\text{Hz}}$  [10], while the limit of traditional receivers is around  $1 \text{ nV/cm}/\sqrt{\text{Hz}}$  [11]. Additionally, a RARE can detect a wide range of frequencies, spanning from the Megahertz (MHz) band to the Terahertz (THz) band [6]. This capability is achieved by exploiting the electron transitions among different energy levels. For example, experiments in [12] have demonstrated the simultaneous detection of 5 RF frequencies spanning from 1.7 GHz to 116 GHz using a single RARE. The detectable frequency range of RAREs can be further expanded by utilizing various quantum techniques to split the energy levels, such as the Zeeman effect and the off-resonant Stark shift [13]–[15].

Researchers have explored RAREs to enhance wireless sensing. Initial efforts have demonstrated their abilities to detect the amplitude and frequency of RF signals via the electromagnetically-induced-transparency (EIT) spectroscopy [16]–[18]. To facilitate the detection of signal phase, the heterodyne sensing technique was subsequently developed [19], [20]. It introduces an extra reference source to transmit a known reference signal to the RARE. The reference signal acts as an *atomic mixer* to down-convert the RF signal to intermediate frequency, facilitating phase detection [21]. Due to its simplified detection procedure, heterodyne sensing has become a mainstream technique for RARE-based wireless sensing. The technique was applied to the subtle vibration monitoring of targets [7]. The experiments show that RARE can improve the sensing accuracy by at least an order of magnitude as compared with traditional Wi-Fi sensing. Another main application of heterodyne sensing is the detection of the angles-of-arrival (AoAs), using an array of RAREs [22], [23]. Compatible signal processing techniques, namely multiple signal classification (MUSIC) and rotational invariant techniques (ESPRIT), have been designed to enhance the AoA estimation accuracy of RARE [24], [25].

Nevertheless, existing heterodyne-sensing techniques face two critical limitations that hinder their implementation in practical wireless sensing systems. Firstly, the extra reference source leads to a bulky architecture, increased hardware cost, and higher energy consumption. Additional signal decoupling between the transmitter and the RARE are also required to mitigate self-interference. Secondly, although a RARE can interact with RF signals across a wide frequency range as mentioned earlier, its detectable instantaneous bandwidth,

The authors are with Department of Electrical and Electronic Engineering, The University of Hong Kong, Hong Kong (Emails: {mycui, qszeng, zhanweiw, huangkb}@eee.hku.hk). Corresponding authors: Q. Zeng; K. Huang.

which refers to the frequency spread of a signal at a given time, is typically no more than 10MHz [26], [27]. This characteristic constrains the maximum bandwidth of the sensing signal and the sensing resolution. The above limitations pose a challenge for quantum heterodyne sensing to support high-resolution wireless sensing tasks, such as ranging in 6G autonomous driving systems.

To overcome these limitations, we propose a novel concept called *self-heterodyne sensing*. The core idea is to utilize the self-interference generated by the transmitted sensing signal as the reference signal. The main contributions of our work are summarized below.

- **Architecture and property of self-heterodyne sensing:**

The proposed architecture modifies that of heterodyne sensing by removing both the transmitter-receiver decoupling and external reference source. It allows the transmitted linear-frequency modulated (LFM) signal itself to serve as both the sensing and reference signals, giving the name “self-heterodyne sensing”. Our first finding reveals a key property of the proposed architecture: a self-heterodyne RARE functions as an *atomic autocorrelator*, where the received signal represents the *autocorrelation of the transmitted signal at different delays*. This characteristic translates the range of a sensing target into the frequency of the received signal, thereby facilitating quantum range sensing through frequency estimation. As another of its key properties, the self-heterodyne architecture, utilizing identical reference and sensing LFM waveforms, allows for precise control of the instantaneous bandwidth of the received signal to fit the detectable bandwidth range of a RARE. In contrast, existing heterodyne sensing techniques lack this control mechanism, as they employ single-frequency reference signals.

- **Algorithmic design for self-heterodyne sensing:** The range sensing problem (i.e., the aforementioned frequency estimation) is formulated as a *nonlinear least square (NLS) problem*. We propose a *two-stage algorithm* to efficiently solve this problem, which comprises a *coarse estimation stage* and a *refinement stage*. The first stage assumes that the time-varying amplitude of received signal varies much more slowly than the phase, allowing the estimation of the target range from the signal frequency. The second stage refines the estimated range using Newton’s method. Numerical results demonstrate that the proposed algorithm for self-heterodyne sensing can approach Cramér-Rao lower bound (CRLB).

- **Sensitivity maximization for self-heterodyne sensing:** We introduce the novel technique of *power-trajectory* ( $P$ -trajectory), aimed at maximizing the sensitivity of RARE by manipulating the time-varying transmission power. This strategy is inspired by the finding that the gain of a self-heterodyne RARE exhibits a *complex pattern with respect to (w.r.t) the transmission power*, making the conventional *fixed power* transmission scheme sub-optimal. To address this issue, we first design a heuristic  $P$ -trajectory by analyzing the asymptotically optimal power that maximizes the sensitivity. It is proven that

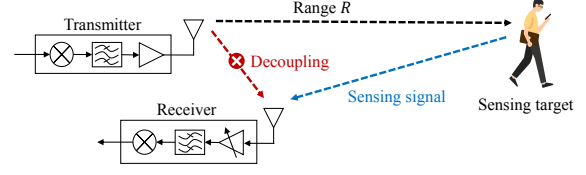


Figure 1. Classic wireless sensing system.

the power should *vary linearly* with the carrier frequency when the reference signal is far off-resonant from the electron transition, whereas the power should *remain constant in the resonant case*. We then extend the heuristic  $P$ -trajectory to practical  $P$ -trajectories by considering the transmission power constraint. Numerical results confirm that the  $P$ -trajectory technique significantly enhances the sensitivity of self-heterodyne sensing.

The remainder of the paper is organized as follows. The classic and quantum wireless sensing systems are reviewed in Section II. The architecture and property of self-heterodyne sensing are introduced in Section III, followed by the two-stage self-heterodyne sensing algorithm in Section IV. Section V elaborates on  $P$ -trajectory design for sensitivity maximization. Numerical experiments are conducted in Section VI, and conclusions are drawn in Section VII.

## II. REVIEW OF EXISTING WIRELESS SENSING PARADIGMS

This section provides preliminaries useful for understanding the proposed designs. We start with an introduction to the basic principles of classic wireless sensing for the purpose of comparison. We then introduce the electron transition model and the heterodyne sensing technique utilized in existing quantum wireless sensing systems.

### A. Review of Classic Wireless Sensing

This paper focuses on the monostatic radar sensing. The architecture of the classic wireless sensing system is depicted in Fig. 1. The transmitter employs the LFM waveform to sense the target range [28], expressed as:

$$s_0(t) = \text{Re}\left\{\sqrt{P_{\text{tx}}}e^{j\vartheta_0(t)}\text{rect}(t/T)\right\}, \quad (1)$$

where the phase modulation function is given as  $\vartheta_0(t) = \frac{1}{2}\alpha t^2 + \omega_0 t$ . The parameters  $P_{\text{tx}}$ ,  $T$ ,  $\omega_0$ , and  $\alpha$  represent the transmission power, symbol duration, start frequency, and sweep slope of the LFM waveform. The rectangular function  $\text{rect}(x)$  equals 1 if  $0 \leq x < 1$  and 0 otherwise. We define  $B = \frac{\alpha T}{2\pi}$  as the sweep bandwidth of the considered LFM waveform. Let  $R > 0$  denote the *target range to be detected*. The *roundtrip propagation time* is  $\tau = \frac{2R}{c}$ , with  $c$  representing the speed of light. The roundtrip channel fading  $h > 0$  is modeled as  $h = \sqrt{\frac{\lambda_0^2 \sigma_S}{4\pi^3 R^4}}$ , where  $\lambda_0 = \frac{2\pi c}{\omega_0}$  is the wavelength corresponding to the start frequency  $\omega_0$ , and  $\sigma_S$  denotes the cross-section of the target [29]. At the classic receiver, the *received baseband complex signal* is expressed as:

$$y_0(t) = \sqrt{P_0 G_0} h e^{j\frac{1}{2}\alpha(t-\tau)^2} \text{rect}((t-\tau)/T) + n_0(t), \quad (2)$$

where  $P_0 = P_{\text{tx}} G_{\text{tx}}$  and  $G_0 = G_{\text{rx}} G_{\text{lna}} G_{\text{rec}}$ . The parameters  $G_{\text{tx}}$ ,  $G_{\text{rx}}$ ,  $G_{\text{lna}}$ , and  $G_{\text{rec}}$  represent the gains of the

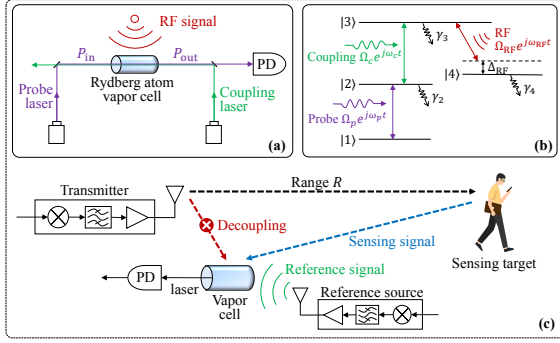


Figure 2. (a) Structure of a RARE; (b) the four-level quantum system; (c) the quantum heterodyne sensing system.

transmit antenna, receive antenna, low-noise amplifier (LNA), and the remaining receiver circuits, respectively. The term  $n_0(t)$  denotes zero-mean Gaussian noise with the property:  $E(n_0(t)n_0^*(t')) = \sigma_0^2 \delta(t - t')$ . The noise power is determined as  $\sigma_0^2 = k_B T_E B$ , where  $k_B$  is the Boltzmann constant and  $T_E$  the equivalent noise temperature. Accordingly, the signal-to-noise ratio (SNR) of  $y_0(t)$  is given as

$$\text{SNR}_0 = P_0 G_0 h^2 / \sigma_0^2 = P_{tx} G_{tx} G_0 h^2 / \sigma_0^2. \quad (3)$$

In the literature, the target range  $R$  can be estimated from the received signal  $y_0(t)$  using a variety of algorithms, such as time-frequency analysis [30] and NLS methods [31]. It is worth noting that the symbol duration,  $T$ , is typically much longer than the roundtrip propagation time,  $\tau$ , (e.g.,  $T = 100 \mu\text{s}$  and  $\tau = 1 \mu\text{s}$  for  $R = 150\text{m}$ ). This disparity implies that the receiver must operate in a “listen-while-transmit” mode, necessitating proper signal decoupling between the transmitter and receiver to mitigate the strong self-interference from the transmitted signal.

### B. Review of Quantum Wireless Sensing

The quantum wireless sensing system uses a RARE in place of traditional RF receivers to capture incident RF signals.

1) *Electron Transition Model*: We first review the electron transition model of RARE. Fig. 2(a) presents the structure of a RARE. A probe laser and a coupling laser propagate in opposite directions through an atom vapor cell to prepare Rydberg atoms. The incident RF signal, carrying information about the target range, changes the quantum states of Rydberg atoms. This interaction results in variations in the power loss of the probe laser as it passes through the vapor cell. By monitoring these variations using a photodetector (PD), the RF signal can be recovered, thereby enabling target sensing.

The quantum response of each Rydberg atom can be characterized by a four-level system, as depicted in Fig. 2(b), which consists of the ground state  $|1\rangle$ , the lowly-excited state  $|2\rangle$ , and the Rydberg states  $|3\rangle$  and  $|4\rangle$ . These states are interconnected by the probe laser, the coupling laser, and the incident RF signal, respectively. Let  $\omega_{ij}$  denote the transition frequency of  $|i\rangle \rightarrow |j\rangle$ , where  $i, j \in \{1, 2, 3, 4\}$ . The probe laser is characterized by a Rabi frequency,  $\Omega_p$ , a carrier frequency,  $\omega_p$ , and a frequency detuning,  $\Delta_p$ . The Rabi frequency  $\Omega_p$  quantifies the strength of the interaction between the probe

laser and the atomic transition. The frequency detuning,  $\Delta_p$ , represents the deviation of the carrier frequency,  $\omega_p$ , from the transition frequency  $\omega_{12}$ , i.e.,  $\Delta_p = \omega_p - \omega_{12}$ . Likewise, we introduce  $\{\Omega_c, \omega_c, \Delta_c = \omega_c - \omega_{23}\}$  for the coupling laser and  $\{\Omega_{RF}, \omega_{RF}, \Delta_{RF} = \omega_{RF} - \omega_{34}\}$  for the RF signal. In this study, both the probe and coupling lasers are set resonant with their respective electron transitions, such that  $\Delta_p = \Delta_c = 0$ .

The quantum state of the considered four-level system is a density matrix  $\rho \in \mathbb{C}^{4 \times 4}$ . The dynamics of  $\rho$  is governed by the Lindblad master equation [20]:

$$\frac{\partial \rho}{\partial t} = -\frac{j}{\hbar} [\mathbf{H}, \rho] + \mathcal{L}, \quad (4)$$

where  $[\mathbf{H}, \rho] = \mathbf{H}\rho - \rho\mathbf{H}$  represents the commutator of the matrix  $\mathbf{H}$  with the matrix  $\rho$ . The matrix,  $\mathbf{H}$ , refers to the system Hamiltonian operator

$$\mathbf{H} = \frac{\hbar}{2} \begin{bmatrix} 0 & \Omega_p & 0 & 0 \\ \Omega_p & 0 & \Omega_c & 0 \\ 0 & \Omega_c & 0 & \Omega_{RF} \\ 0 & 0 & \Omega_{RF} & -2\Delta_{RF} \end{bmatrix}, \quad (5)$$

where  $\hbar$  denotes the reduced Planck constant. The operator  $\mathcal{L}$  indicates the relaxation of the system,

$$\mathcal{L} = \begin{bmatrix} \gamma_2 \rho_{22} + \gamma_4 \rho_{44} & -\frac{\gamma_2}{2} \rho_{12} & -\frac{\gamma_3}{2} \rho_{13} & -\frac{\gamma_4}{2} \rho_{14} \\ -\frac{\gamma_2}{2} \rho_{21} & \gamma_3 \rho_{33} - \gamma_2 \rho_{22} & -\frac{\gamma_3}{2} \rho_{23} & -\frac{\gamma_4}{2} \rho_{24} \\ -\frac{\gamma_3}{2} \rho_{31} & -\frac{\gamma_3}{2} \rho_{32} & -\gamma_3 \rho_{33} & -\frac{\gamma_3}{2} \rho_{34} \\ -\frac{\gamma_4}{2} \rho_{41} & -\frac{\gamma_4}{2} \rho_{42} & -\frac{\gamma_4}{2} \rho_{43} & -\gamma_4 \rho_{44} \end{bmatrix}$$

Here,  $\gamma_{ij} = (\gamma_i + \gamma_j)$ , where  $\gamma_i$  ( $i = 2, 3, 4$ ) is the decay rate. We are interested in the steady-state (when  $\frac{\partial \rho}{\partial t} = 0$ ) solution of  $\rho_{12}$  as it is associated with the probe laser to be measured, which is proven to be [32]

$$\rho_{12} = \frac{A_1 \Omega_{RF}^2 \Delta_{RF}^2 + j B_1 \Omega_{RF}}{C_1 \Omega_{RF}^4 + C_2 \Omega_{RF}^2 + C_3 \Delta_{RF}^2}. \quad (6)$$

Here,  $A_1 = 2\Omega_p \Omega_c^2$ ,  $B_1 = \gamma_2 \Omega_p$ ,  $C_1 = 2\Omega_p^2 + \gamma_2^2$ ,  $C_2 = 2\Omega_p^2 (\Omega_c^2 + \Omega_p^2)$ , and  $C_3 = 4(\Omega_c^2 + \Omega_p^2)^2$ .

According to the adiabatic approximation, the power of the probe laser coming out of the vapor cell is determined by the imaginary part of  $\rho_{12}$  [20]:

$$P_{\text{out}} = P_{\text{in}} \exp(-C_0 \text{Im}\{\rho_{12}\}), \quad (7)$$

where  $P_{\text{in}}$  denotes the input power of the probe laser. The constant  $C_0$  is given as  $C_0 \triangleq \frac{2N_0 \mu_{12}^2 k_p L}{\epsilon_0 \hbar \Omega_p}$ , where  $N_0$  represents the total density of atoms,  $\mu_{12}$  the dipole moment associated with the transition  $|1\rangle \rightarrow |2\rangle$ ,  $\epsilon_0$  the vacuum permittivity,  $L$  the length of vapor cell, and  $k_p$  the wavenumber of probe laser. For brevity, we introduce the function

$$\Pi(\Omega, \Delta) \triangleq P_{\text{in}} \exp \left\{ -\frac{B_1 C_0 \Omega^4}{C_1 \Omega^4 + C_2 \Omega^2 + C_3 \Delta^2} \right\}, \quad (8)$$

with  $\Omega \in [0, +\infty)$  and  $\Delta \in \mathbb{R}$ , to rewrite the probe-laser power  $P_{\text{out}}$  as  $\Pi(\Omega_{RF}, \Delta_{RF})$ . For ease of future usage, we also define the partial derivative of  $\Pi(\Omega, \Delta)$  w.r.t  $\Omega$  as

$$\Upsilon(\Omega, \Delta) \triangleq \frac{\partial \Pi(\Omega, \Delta)}{\partial \Omega} = -2P_{\text{in}} B_1 C_0 \times \exp \left\{ -\frac{B_1 C_0 \Omega^4}{C_1 \Omega^4 + C_2 \Omega^2 + C_3 \Delta^2} \right\} \frac{\Omega^3 (C_2 \Omega^2 + 2C_3 \Delta^2)}{(C_1 \Omega^4 + C_2 \Omega^2 + C_3 \Delta^2)^2}. \quad (9)$$

2) *Heterodyne sensing*: To accurately extract target information from the RF signal, the heterodyne sensing technique is

commonly employed [19], [20]. This technique, as illustrated in Fig. 2(c), introduces an additional reference source near the RARE. The reference source emits a reference signal to the RARE, which interferes with the sensing signal reflected by the target to form the incident RF signal. **Notably, the reference signal needs to be much stronger than the sensing signal and its waveform should be known to the RARE.**

In the literature, the reference signal is usually a sinusoidal signal, used to lock the transition frequency of RARE. We represent the transmitted reference signal as  $\text{Re}\{\sqrt{P_{r,\text{tx}}}e^{j\omega_r t}\}$ , where  $P_{r,\text{tx}}$  denotes the transmission power and  $\omega_r$  the carrier frequency. The received reference signal is thus

$$E_r(t) = \text{Re}\left\{\sqrt{P_r}e^{j(\omega_r t - \omega_r \tau')}\right\}, \quad (10)$$

where  $P_r$  denotes the received power,  $\tau'$  the propagation delay from the reference source to RARE. Therein, the frequency detuning of  $E_r(t)$  is calculated as  $\Delta_r = \omega_r - \omega_{34}$ . The Rabi frequency of  $E_r(t)$ , characterizing the strength of interaction between the reference signal  $E_r(t)$  and electron transition, is expressed as  $\Omega_r = \frac{\mu_{34}}{\hbar} |\sqrt{P_r}e^{j(\omega_r t - \omega_r \tau')}| = \frac{\mu_{34}}{\hbar} \sqrt{P_r}$ , where  $\mu_{34}$  stands for the dipole moment of the transition  $|3\rangle \rightarrow |4\rangle$ .

As for the transmitted sensing signal, it is expressed in a general form,  $\text{Re}\{\sqrt{P_{s,\text{tx}}}e^{j\vartheta_s(t)}\}$ , to deal with different sensing tasks, where  $P_{s,\text{tx}}$  denotes the transmission power and  $\vartheta_s(t)$  a general **time-varying phase function**. Accordingly, the received sensing signal is

$$E_s(t) = \text{Re}\left\{\sqrt{P_s}e^{j\vartheta_s(t-\tau)}\right\}, \quad (11)$$

where  $P_s$  denotes the received power and  $\tau$  the roundtrip propagation time to be estimated. Likewise, the Rabi frequency of  $E_s(t)$  is  $\Omega_s = \frac{\mu_{34}}{\hbar} |\sqrt{P_s}e^{j\vartheta_s(t-\tau)}| = \frac{\mu_{34}}{\hbar} \sqrt{P_s}$ .

As a result, the overall incident RF signal is the superposition of the reference and sensing signals,

$$E_{\text{RF}}(t) = \text{Re}\left\{\sqrt{P_r}e^{j(\omega_r t - \omega_r \tau')} + \sqrt{P_s}e^{j\vartheta_s(t-\tau)}\right\}. \quad (12)$$

The overall Rabi frequency  $\Omega_{\text{RF}}(t)$  is obtained as

$$\begin{aligned} \Omega_{\text{RF}}(t) &= \frac{\mu_{34}}{\hbar} \left| \sqrt{P_r}e^{j(\omega_r t - \omega_r \tau')} + \sqrt{P_s}e^{j\vartheta_s(t-\tau)} \right| \\ &= |\Omega_r + \Omega_s e^{j\vartheta_{sr}(t;\tau,\tau')}|, \end{aligned} \quad (13)$$

where  $\vartheta_{sr}(t;\tau,\tau') \triangleq \vartheta_s(t-\tau) - \omega_r t + \omega_r \tau'$ . **Moreover, as the reference signal is much stronger than the sensing signal,  $P_r \gg P_s$ , the overall frequency detuning,  $\Delta_{\text{RF}}$ , is largely determined by that of the reference signal**

$$\Delta_{\text{RF}} = \Delta_r = \omega_r - \omega_{34}. \quad (14)$$

By substituting (13) and (14) into the output power of the probe laser,  $P_{\text{out}} = \Pi(\Omega_{\text{RF}}, \Delta_{\text{RF}})$ , and taking the noise into account, the **measured signal at the PD** is given as

$$\begin{aligned} y(t) &= \Pi(|\Omega_r + \Omega_s e^{j\vartheta_{sr}(t;\tau,\tau')}|, \Delta_r) + n(t) \\ &\stackrel{(a)}{\approx} \underbrace{\Pi(\Omega_r, \Delta_r)}_{\text{bias}} + \underbrace{\frac{\mu_{34}}{\hbar} \Upsilon(\Omega_r, \Delta_r) \sqrt{P_s}}_{\text{gain}} \underbrace{\cos(\vartheta_{sr}(t;\tau,\tau'))}_{\text{oscillation term}} + \underbrace{n(t)}_{\text{noise}}, \end{aligned} \quad (15)$$

where the linearization (a) comes from the first-order Taylor expansion of  $\Pi(\Omega_{\text{RF}}, \Delta_r)$  when  $P_r \gg P_s$ . The terms  $\Pi(\Omega_r, \Delta_r)$  and  $\frac{\mu_{34}}{\hbar} \Upsilon(\Omega_r, \Delta_r)$  represent the direct-current bias of the probe-laser power and the amplification gain of

RARE, respectively. The zero-mean Gaussian noise  $n(t)$ , with  $E(n(t')n(t)) = \sigma^2 \delta(t-t')$ , mainly comes from the photon shot noise (PSN) of the PD [5], whose covariance is

$$\sigma^2 = \Pi(\Omega_r, \Delta_r)KB, \quad (16)$$

The parameter  $K$  is expressed as  $K = \frac{\hbar\omega_p}{R\eta}$ , where  $\omega_p$  denotes the angular frequency of the probe laser,  $R$  the resistance of PD, and  $\eta$  the quantum efficiency of PD. The signal model in (15) reveals **that the reference signal acts as a down-converter with a down-conversion frequency of  $\omega_r$** . Henceforth, a heterodyne-sensing RARE is also regarded as an atomic mixer [19]. By manipulating the waveform of sensing signal,  $e^{j\vartheta_s(t)}$ , the RARE is able to conduct diverse sensing tasks. Below are two examples illustrating this capability.

*Example 1* ( $\vartheta_s(t) = \omega_s t$ ): When  $\vartheta_s(t) = \omega_s t$ , the received waveform is  $y(t) \propto \cos((\omega_s - \omega_r)t - \omega_s \tau + \omega_r \tau')$ . The target range,  $R$ , can be recovered from the phase of probe laser,  $-\omega_s \tau + \omega_r \tau' = -\omega_s \frac{2R}{c} + \omega_r \tau'$ , by compensating for the phase of the known reference signal,  $\omega_r \tau'$ . However, due to phase ambiguity, a distinguishable range,  $R$ , must satisfy  $\omega_s \tau = \frac{2R\omega_s}{c} < 2\pi$ . For a typical WiFi signal with  $\omega_s = 2\pi \times 1.5\text{GHz}$ , we have  $R < 0.1\text{m}$ . **This implies that for a single-frequency sensing signal, the RARE is suitable for sensing target ranges on a small scale, such as micro-vibrations [7].**

*Example 2* ( $\vartheta_s(t) = \frac{1}{2}\alpha t^2 + \omega_0 t$ ): This paper focuses on sensing target ranges on a larger scale, e.g.,  $R \in [1\text{m}, 1000\text{m}]$ . By using the LFM waveform,  $\vartheta_s(t) = \vartheta_0(t) = \frac{1}{2}\alpha t^2 + \omega_0 t$ , as commonly used in classic wireless sensing, the phase ambiguity issue can be effectively addressed [28], [29]. With the LFM waveform, the received waveform is expressed as  $y(t) \propto \cos(\frac{1}{2}\alpha(t-\tau)^2 + \omega_0(t-\tau) - \omega_r(t-\tau'))$ . This enables the recovery of the range  $R$  from  $y(t)$  using **time-frequency analysis algorithms**.

### C. Implementation Challenges of Heterodyne Sensing

Although the heterodyne sensing technique exhibits high sensitivity, it faces two critical challenges in implementation.

1) *Bulky transceiver architecture*: Heterodyne sensing requires a bulky transceiver architecture. As presented in Fig. 2(c), an external reference source must be deployed, leading to increased hardware cost and energy consumption. Furthermore, ensuring proper signal decoupling between the transmitter and RARE is essential to mitigate self-interference, which entails additional hardware and algorithm costs.

2) *Insufficient instantaneous bandwidth*: To satisfy the minimum resolution requirement of range sensing, the sweep bandwidth,  $B$ , of the LFM signal in *Example 2* needs to be at least tens of MHz [33]. However, while the detectable frequency range of a RARE is wide due to the abundant energy levels, **the detectable instantaneous bandwidth of RARE typically does not exceed 10 MHz [27]. This limitation results from the long response time needed for the quantum state  $\rho_{12}$  to become steady.** The mismatch between the required sweep bandwidth,  $B$ , and the limited instantaneous bandwidth of RARE hinders the application of existing heterodyne-sensing techniques in high-resolution range sensing.



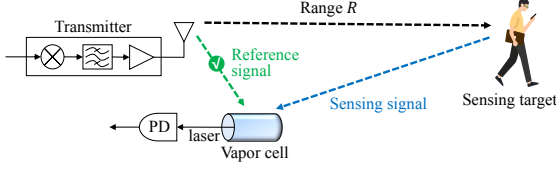


Figure 3. The proposed quantum self-heterodyne sensing system.

### III. SELF-HETERODYNE SENSING: ARCHITECTURE AND PROPERTIES

To address the implementation challenges of heterodyne sensing, we propose the concept of *self-heterodyne sensing* for RAREs. Its key idea is to utilize the self-interference generated by the transmitted sensing signal as the reference signal. This approach is motivated by two factors: 1) In monostatic sensing where the transmitter is in close proximity to the RARE, the self-interference signal can be as strong as the reference signal. 2) The waveform of the transmitted signal is already known to the RARE in sensing applications. With these considerations, the transmitted signal itself is a perfect alternative to the reference, enabling the elimination of the transmitter-receiver decoupling and the external reference source.

In this section, we first introduce the architecture of self-heterodyne sensing. Subsequently, a comprehensive discussion on the properties of self-heterodyne is conducted to show its superiority over existing heterodyne sensing techniques.

#### A. Architecture of Self-Heterodyne Sensing

The architecture of self-heterodyne sensing is depicted in Fig. 3, which comprises a classical transmitter, a RARE, and the target to be sensed. The transmitter broadcasts a signal towards the RARE and the target simultaneously. The signal component that directly reaches the RARE acts as the reference signal for assisting signal detection. The signal component directed towards the target is reflected back and serves as the sensing signal. Details regarding the architecture are provided below.

1) *Transmitted signal*: To enable high-resolution range sensing, we continue to use the LFM transmitted signal

$$s(t) = \text{Re}\left\{\sqrt{P_{\text{tx}}(t)}e^{j\vartheta_s(t)}\text{rect}(t/T)\right\}, \quad (17)$$

where  $\vartheta_s(t) = \vartheta_0(t) = \frac{1}{2}\alpha t^2 + \omega_0 t$ . Different from the LFM waveform adopted in [1] with a fixed transmission power  $P_{\text{tx}}$ , we consider a more general LFM waveform in [17]. It allows the transmission power,  $P_{\text{tx}}(t)$ , to be time-varying. This design aims at enhancing the sensitivity of RARE, which will be elaborated in Section V. We assume that the power  $P_{\text{tx}}(t)$  varies much more slowly than the phase  $\vartheta_s(t)$ . Therefore, the instantaneous frequency of  $s(t)$  is still  $\frac{d\vartheta_s(t)}{dt} = \alpha t + \omega_0$ .

2) *Received sensing signal*: The received sensing signal at the RARE comes from the transmitted signal that is reflected by the target, which is expressed as

$$E_s(t) = \text{Re}\left\{\sqrt{P_{\text{tx}}(t-\tau)G_{\text{tx}}'}h'e^{j\vartheta_s(t-\tau)}\text{rect}[(t-\tau)/T]\right\} \\ \stackrel{(a)}{\approx} \text{Re}\left\{\sqrt{P_s(t)}e^{j\vartheta_s(t-\tau)}\text{rect}(t/T)\right\}. \quad (18)$$

Here,  $P_s(t) = P_{\text{tx}}(t)G_{\text{tx}}'h'^2$  is the received power, where  $G_{\text{tx}}$  represents the transmit antenna gain pertaining to the transmitter-to-target link. The approximation (a) holds because  $T \gg \tau$  and  $P_{\text{tx}}(t)\text{rect}(t/T)$  varies very slowly. The Rabi frequency of  $E_s(t)$  that describes the strength of interaction between the sensing signal  $E_s(t)$  and electron transition is clearly  $\Omega_s(t) = \left|\frac{\mu_{34}}{\hbar}\sqrt{P_s(t)}e^{j\vartheta_s(t-\tau)}\right| = \frac{\mu_{34}}{\hbar}\sqrt{P_{\text{tx}}(t)G_{\text{tx}}'}h'$ .

3) *Received reference signal*: Likewise, the reference signal impinging on the RARE is also a delayed version of the transmitted signal  $s(t)$ :

$$E_r(t) = \text{Re}\left\{\sqrt{P_{\text{tx}}(t-\tau')G_{\text{tx}}'}h'e^{j\vartheta_s(t-\tau')}\text{rect}[(t-\tau')/T]\right\} \\ \approx \text{Re}\left\{\sqrt{P_r(t)}e^{j\vartheta_s(t-\tau')}\text{rect}(t/T)\right\}, \quad (19)$$

where  $P_r(t) = P_{\text{tx}}(t)G_{\text{tx}}'h'^2$ . The parameters  $h'$ ,  $\tau'$ , and  $G_{\text{tx}}'$  refer to the path loss, propagation delay, and transmit antenna gain of the transmitter-to-RARE link. Note that  $G_{\text{tx}}'$  differs from  $G_{\text{tx}}$  because the transmitter-to-target and transmitter-to-RARE links have different directions. The Rabi frequency associated with the signal,  $E_r(t)$ , is thus  $\Omega_r(t) = \left|\frac{\mu_{34}}{\hbar}\sqrt{P_r(t)}e^{j\vartheta_s(t-\tau')}\right| = \frac{\mu_{34}}{\hbar}\sqrt{P_{\text{tx}}(t)G_{\text{tx}}'}h'$ .

4) *Overall incident RF signal*: Similar to [12], the overall incident RF signal is the superposition of  $E_s(t)$  and  $E_r(t)$ :

$$E_{\text{RF}}(t) = E_s(t) + E_r(t) \\ = \text{Re}\left\{\sqrt{P_s(t)}e^{j\vartheta_s(t-\tau)} + \sqrt{P_r(t)}e^{j\vartheta_s(t-\tau')}\right\}\text{rect}(t/T). \quad (20)$$

Since we mainly focus on the time period  $t \in [0, T]$  when  $\text{rect}(t/T) = 1$ , the term  $\text{rect}(t/T)$  can be safely omitted in the subsequent discussions without loss of generality. Leveraging the expressions of  $\Omega_s(t)$ ,  $\Omega_r(t)$ , and  $E_{\text{RF}}(t)$ , we can derive the Rabi frequency associated with the incident RF signal as

$$\Omega_{\text{RF}}(t) = \frac{\mu_{34}}{\hbar}\left|\sqrt{P_r(t)}e^{j\vartheta_s(t-\tau')} + \sqrt{P_s(t)}e^{j\vartheta_s(t-\tau)}\right| \\ = |\Omega_r(t) + \Omega_s(t)e^{j\vartheta_{ss}(t;\tau,\tau')}|. \quad (21)$$

Here, the phase function  $\vartheta_{ss}(t; \tau, \tau')$  is defined as

$$\vartheta_{ss}(t; \tau, \tau') = \vartheta_s(t-\tau) - \vartheta_s(t-\tau') = -\omega t - \varphi, \quad (22)$$

where  $\omega \triangleq (\tau - \tau')\alpha$  and  $\varphi \triangleq \frac{1}{2}(\tau - \tau')(\omega_0 - \tau - \tau')\alpha$ . Regarding the overall frequency detuning,  $\Delta_{\text{RF}}$ , it is still determined by the strong reference signal,  $E_r(t)$ , similar to the heterodyne sensing scheme. However, a major difference from the detuning of heterodyne sensing, as depicted in [14], is that the carrier frequency of the reference signal in [19] is no longer fixed but time-varying. This characteristic makes the frequency detuning of self-heterodyne sensing time-varying as well. Specifically, the instantaneous frequency of the reference signal in [19] is given by  $\frac{d\vartheta_s(t-\tau')}{dt}$ . The frequency detuning should be thus adjusted from [14] to

$$\Delta_{\text{RF}}(t) = \Delta_r(t) = \frac{d\vartheta_s(t-\tau')}{dt} - \omega_{34} = \alpha t + \gamma, \quad (23)$$

where  $\gamma \triangleq -\alpha\tau' + \omega_0 - \omega_{34}$ .

5) *Measured probe-laser power*: By substituting [21] and [23] into  $P_{\text{out}}(t) = P_{\text{in}}e^{C_0 \text{Im}\{\rho_{21}(t)\}} = \Pi(\Omega_{\text{RF}}, \Delta_{\text{RF}})$ , we

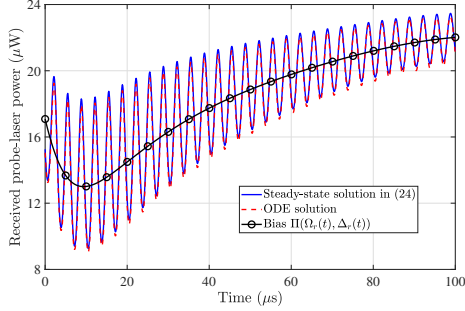


Figure 4. The evolution of the measured probe-laser power  $y(t)$  in the absence of noise. Some key parameters are listed below:  $\Omega_p = 2\pi \times 6$  MHz,  $\Omega_c = 2\pi \times 10$  MHz,  $\Omega_r(t) = 2\pi \times 2\sqrt{1+5t/T}$  MHz,  $\Omega_s(t) = 2\pi \times 0.1\sqrt{1+5t/T}$  MHz,  $B = 40$  MHz,  $T = 100$   $\mu$ s, and  $\tau - \tau' = 0.75$   $\mu$ s.

can express the measured probe-laser power as:

$$y(t) = \Pi(|\Omega_r(t) + \Omega_s(t)e^{j\vartheta_{ss}(t;\tau,\tau')}|, \Delta_r(t)) + n(t) \\ \stackrel{(a)}{\approx} \underbrace{\Pi(\Omega_r(t), \Delta_r(t))}_{\text{time-varying bias}} + \underbrace{\frac{\mu_{34}}{\hbar} \Upsilon(\Omega_r(t), \Delta_r(t))}_{\text{time-varying gain}} \\ \times \sqrt{P_s(t)} \cos(\vartheta_{ss}(t;\tau,\tau')) + n(t), \quad (24)$$

where (a) comes from the first-order Taylor expansion of  $\Pi(\Omega_{RF}(t), \Delta_r(t))$  with  $\Omega_r(t) \gg \Omega_s(t)$ . The power of the zero-mean Gaussian noise  $n(t)$ , with  $E(n(t')n(t)) = \sigma^2(t)\delta(t-t')$ , is proportional to  $\Pi(\Omega_r(t), \Delta_r(t))$ :

$$\sigma^2(t) = \Pi(\Omega_r(t), \Delta_r(t))KB. \quad (25)$$

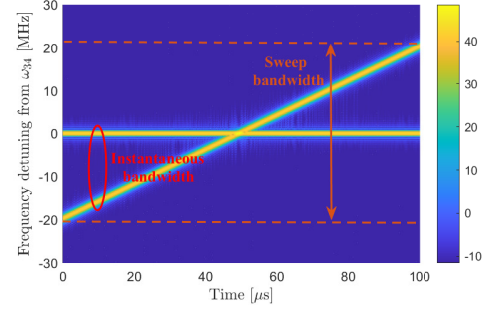
The signal model in [24] reveals that the proposed self-heterodyne sensing strategy can naturally convert the target range,  $R = \frac{c\tau}{2}$ , into the phase difference function  $\vartheta_{ss}(t;\tau,\tau') = -\omega t - \varphi$ . This conversion allows the detection of target range via estimating the fluctuation frequency of the probe-laser power,  $\omega = (\tau - \tau')\alpha$ .

An example of the measured probe-laser power,  $y(t)$ , in the absence of noise is presented in Fig. 4. The curve labeled as “ODE solution” is computed using the RydQuLe software [34], an open-source Rydberg sensor simulator. It uses ordinary differential equation (ODE) solvers to numerically solve the Lindblad master equation in (4), providing accurate dynamics of  $\rho_{21}(t)$  and  $y(t)$ . The derived steady-state solution of the probe-laser power in (24) closely aligns with the ODE solution. Both solutions exhibit fluctuations around the time-varying bias  $\Pi(\Omega_r(t), \Delta_r(t))$ , with an equal frequency of  $(\tau - \tau')\alpha$ . This observation confirms the efficacy and accuracy of the derived signal model in self-heterodyne sensing.

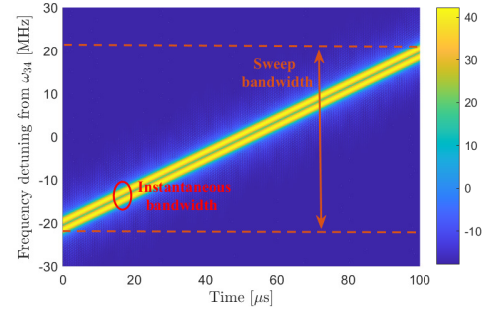
### B. Properties of Self-heterodyne Sensing

We now elaborate on the unique properties and advantages of self-heterodyne sensing.

1) *Transceiver architecture*: The transceiver architecture of self-heterodyne sensing is much simpler than that of heterodyne sensing. The additional reference source as well as the signal decoupling between the transmitter and RARE, which are essential components in heterodyne sensing, are no longer needed in self-heterodyne sensing.



(a) Heterodyne-sensing with  $\vartheta_s(t) = \frac{1}{2}\alpha t^2 + \omega_0 t$ .



(b) Self-heterodyne-sensing with  $\vartheta_s(t) = \frac{1}{2}\alpha t^2 + \omega_0 t$ .

Figure 5. STFT of incident RF signals. The parameters are as follows:  $T = 100$   $\mu$ s,  $\tau' = 10$  ns,  $\tau = 5$   $\mu$ s,  $B = 40$  MHz, and  $\omega_0 = \omega_r = 3.5$  GHz.

2) *Signal model*: In the signal model of heterodyne sensing as depicted in [15], the phase function of received signal is determined by the waveform of sensing signal down-converted by the carrier frequency of reference signal, i.e.,  $\vartheta_{sr}(t;\tau,\tau') = \vartheta_s(t-\tau) - \omega_r t + \omega_r \tau'$ . In contrast, for self-heterodyne sensing, the phase function of received signal is the difference between the phase functions of the transmitted signal with two distinct delays, i.e.,  $\vartheta_{ss}(t;\tau,\tau') = \vartheta_s(t-\tau) - \vartheta_s(t-\tau')$ . This representation captures exactly the autocorrelation of the transmitted signal. The comparison above highlights the physical distinctions between heterodyne RARE and self-heterodyne RARE. The former can be viewed as *atomic mixer* [19], while the latter functions as an *atomic autocorrelator*.

Moreover, in the heterodyne sensing signal model, the bias  $\Pi(\Omega_r, \Delta_r)$ , the gain  $\frac{\mu_{34}}{\hbar} \Upsilon(\Omega_r, \Delta_r)$ , and the noise power  $\sigma^2$  are time-invariant due to the fixed frequency detuning of the reference signal. However, in self-heterodyne sensing, as the carrier frequency of reference signal is time-varying, the above parameters become time-varying as well, denoted as  $\Pi(\Omega_r(t), \Delta_r(t))$ ,  $\frac{\mu_{34}}{\hbar} \Upsilon(\Omega_r(t), \Delta_r(t))$ , and  $\sigma^2(t)$ .

3) *Bandwidth*: Self-heterodyne sensing can support a much wider sweep bandwidth,  $B$ , compared to heterodyne sensing. This is because the atomic autocorrelator enables the control of the instantaneous bandwidth of the received signal to fit the detectable bandwidth range of a RARE, as elaborated below.

In the context of a classical atomic mixer realized by heterodyne sensing, the incident RF signal described in [12] consists of a single-frequency reference signal and a LFM sensing signal. Fig. 5(a) visualizes the Short-Time-Fourier-Transform

(STFT) of this RF signal [35]. The frequency gap between the LFM component and the single-frequency component varies linearly over time. Particularly, the instantaneous bandwidth of the incident RF signal can expand from 0 to half of the sweep bandwidth,  $B/2$ , as time going by. In a typical wireless sensing application,  $B$  can range from tens of MHz to tens of GHz. Unfortunately, it is challenging for a RARE to detect such a broad instantaneous bandwidth.

In the proposed atomic autocorrelator implemented by self-heterodyne sensing, the incident RF signal in (20) is the superposition of two identical waveforms with different delays,  $\tau$  and  $\tau'$ . This configuration ensures that the frequency gap between the two signal components remains unchanged over time, resulting in a constant and narrow instantaneous bandwidth. The STFT of RF signal is plotted in Fig. 5(b). Despite having a broad sweep bandwidth, the RF signal only occupies a narrow frequency range instantaneously due to the identical reference and sensing waveforms. Mathematically, the instantaneous bandwidth of the received signal in (24) is given as  $\frac{\omega}{2\pi} = \frac{(\tau-\tau')\alpha}{2\pi} = \frac{\tau-\tau'}{T}B$ . As the symbol duration  $T$  is a controllable parameter, we can properly set its value to make  $\frac{\tau-\tau'}{T}B$  fall within the detectable bandwidth range of a RARE. For instance, consider typical values in wireless sensing,  $\tau = 1 \mu\text{s}$ ,  $\tau' = 1 \text{ ns}$ , and  $T = 100 \mu\text{s}$ . The instantaneous bandwidth occupies just 1% of the sweep bandwidth,  $B$ . Thereafter, the proposed self-heterodyne sensing is more suitable for RARE in high-resolution wireless sensing.

#### IV. SELF-HETERODYNE SENSING: ALGORITHMIC DESIGN

In this section, we first formulate the range detection problem in self-heterodyne sensing as a NLS problem. Then, a two-stage algorithm is designed to solve the formulated problem. This algorithm involves a coarse estimation stage based on spectrum analysis followed by a refinement stage using Newton's method. Lastly, the CRLB for self-heterodyne sensing will be analyzed.

##### A. NLS Problem Formulation

To ease the discussion, we normalize the received signal as

$$\begin{aligned}\bar{y}(t) &= (y(t) - \Pi(\Omega_r(t), \Delta_r(t))) / \sigma(t) \\ &= \varrho(t)h \cos(\omega t + \varphi) + \bar{n}(t),\end{aligned}\quad (26)$$

where the equivalent Gaussian noise  $\bar{n}(t)$  has unit power, and the time-varying amplitude  $\varrho(t)$  is defined as

$$\varrho(t) = \frac{\mu_{34}\Upsilon(\Omega_r(t), \Delta_r(t))\sqrt{P_{\text{tx}}(t)G_{\text{tx}}}}{h\sqrt{\Pi(\Omega_r(t), \Delta_r(t))KB}}. \quad (27)$$

As the relative position from the transmitter to the RARE is fixed, the parameters of the reference signal,  $\Omega_r(t)$  and  $\Delta_r(t)$ , and the time-varying amplitude,  $\varrho(t)$ , can be acquired in advance. Conversely, the channel parameters pertaining to the target, i.e.,  $h$ ,  $\tau$ , and  $\varphi$ , are unknown to RARE and should be estimated. As the target range,  $R$ , is embedded in the frequency of the received probe-laser power,  $\omega = (\tau - \tau')\alpha = (\frac{R}{2c} - \tau')\alpha$ , the range sensing problem is equivalently a

frequency estimation problem with a time-varying amplitude,  $\varrho(t)$ . We adopt the NLS principle to formulate it as

$$\min_{\hat{h}, \hat{\omega}, \hat{\varphi}} \int_0^T |\bar{y}(t) - \varrho(t)\hat{h} \cos(\hat{\omega}t + \hat{\varphi})|^2 dt, \quad (28)$$

Solving problem (28), we can estimate the target range as  $\hat{R} = 2c(\hat{\omega}/\alpha + \tau')$ .

##### B. NLS Algorithm

We first seek the optimal solution for  $\hat{h}$  in the formulated NLS problem. By setting the derivative of (28) w.r.t  $\hat{h}$  to zero, the optimal  $\hat{h}$  can be obtained straightforwardly as

$$\hat{h} = \frac{\int_0^T \bar{y}(t)\varrho(t) \cos(\hat{\omega}t + \hat{\varphi}) dt}{\int_0^T |\varrho(t) \cos(\hat{\omega}t + \hat{\varphi})|^2 dt}. \quad (29)$$

By further substituting (29) into (28), the original NLS problem is transformed to

$$\max_{\hat{\omega}, \hat{\varphi}} Q(\hat{\omega}, \hat{\varphi}) \triangleq \frac{\left| \int_0^T \bar{y}(t)\varrho(t) \cos(\hat{\omega}t + \hat{\varphi}) dt \right|^2}{\int_0^T |\varrho(t) \cos(\hat{\omega}t + \hat{\varphi})|^2 dt}, \quad (30)$$

which is clearly a non-convex programming. Finding its global optimal solution requires a high-complexity two-dimensional search over the frequency and phase plane. We devise a two-stage algorithm to address (30) with low complexity, which involves a coarse estimation stage followed by a refinement stage. The first stage aims at finding good initial estimates,  $\hat{\omega}^{(0)}$  and  $\hat{\varphi}^{(0)}$ , efficiently, while the refinement stage fine-tunes  $\hat{\omega}$  and  $\hat{\varphi}$  to approach the global optimal solution. The step-by-step procedures are presented below.

1) *Coarse estimation stage*: The first stage assumes that the cosine term  $\cos(\hat{\omega}t + \hat{\varphi})$  in  $Q(\hat{\omega}, \hat{\varphi})$  fluctuates much faster than the amplitude term  $|\varrho(t)|^2$ . Harnessing this assumption, the denominator in (30) can be approximated as

$$\begin{aligned}\int_0^T |\varrho(t) \cos(\hat{\omega}t + \hat{\varphi})|^2 dt &= \frac{1}{2} \int_0^T |\varrho(t)|^2 dt \\ &- \frac{1}{2} \int_0^T |\varrho(t)|^2 \cos(2\hat{\omega}t + 2\hat{\varphi}) dt \approx \frac{1}{2} \int_0^T |\varrho(t)|^2 dt.\end{aligned}\quad (31)$$

Using (31), the problem (30) can be simplified as

$$\max_{\hat{\omega}^{(0)}, \hat{\varphi}^{(0)}} \left| \int_0^T \bar{y}(t)\varrho(t) \cos(\hat{\omega}^{(0)}t + \hat{\varphi}^{(0)}) dt \right|^2. \quad (32)$$

The initial estimated phase,  $\hat{\varphi}^{(0)}$ , can thus be attained by setting the derivative of (32) w.r.t  $\hat{\varphi}^{(0)}$  to zero:

$$\tan(\hat{\varphi}^{(0)}) = -\frac{\int_0^T \bar{y}(t)\varrho(t) \sin(\hat{\omega}^{(0)}t) dt}{\int_0^T \bar{y}(t)\varrho(t) \cos(\hat{\omega}^{(0)}t) dt}. \quad (33)$$

Then, by substituting (33) back to (32) and conducting some tedious calculations, we can rewrite the problem (32) as

$$\max_{\hat{\omega}^{(0)}} \left| \int_0^T \bar{y}(t)\varrho(t) e^{j\hat{\omega}^{(0)}t} dt \right|^2. \quad (34)$$

One can observe from (30) and (34) that the original two-dimensional optimization problem is transferred to a simpler one-dimensional one. In particular, problem (34) is aimed at searching the principal frequency component,  $\hat{\omega}^{(0)}$ , inside

the signal  $\bar{y}(t)\varrho(t)\text{rect}(\frac{t}{T})$ . Therefore, it can be efficiently solved using spectrum analysis tools, such as the Fast Fourier Transform (FFT) technique.

2) *Refinement stage*: The assumption we made in (31) might lead to inaccurate estimate of the target range. To address this issue, we introduce the refinement stage. It iteratively fine-tunes the parameters,  $\hat{\omega}^{(0)}$  and  $\hat{\varphi}^{(0)}$ , obtained in the first stage to maximize the original objective function,  $Q(\hat{\omega}, \hat{\varphi})$ , in (30). We use the superscript  $(i)$  to label the parameters,  $\hat{\omega}^{(i)}$  and  $\hat{\varphi}^{(i)}$ , obtained in the  $i$ -th iteration. The refinement is conducted using the Newton's method, expressed as

$$\begin{pmatrix} \hat{\omega}^{(i)} \\ \hat{\varphi}^{(i)} \end{pmatrix} = \begin{pmatrix} \hat{\omega}^{(i-1)} \\ \hat{\varphi}^{(i-1)} \end{pmatrix} + \begin{pmatrix} \frac{\partial^2 Q}{\partial \hat{\omega}^2} & \frac{\partial^2 Q}{\partial \hat{\omega} \partial \hat{\varphi}} \\ \frac{\partial^2 Q}{\partial \hat{\varphi} \partial \hat{\omega}} & \frac{\partial^2 Q}{\partial \hat{\varphi}^2} \end{pmatrix}^{-1} \begin{pmatrix} \frac{\partial Q}{\partial \hat{\omega}} \\ \frac{\partial Q}{\partial \hat{\varphi}} \end{pmatrix}.$$

We accept a refinement only if the value of the new objective function  $Q(\hat{\omega}^{(i)}, \hat{\varphi}^{(i)})$  is larger than the old one by a threshold.

After the Newton refinement converges, the estimated target range is determined as  $\hat{R} = 2c(\hat{\omega}^{(N_{\text{iter}})}/\alpha + \tau')$ , where  $N_{\text{iter}}$  denotes the total number of iterations.

### C. CRLB Analysis

We now analyze the CRLB of self-heterodyne sensing, as it characterizes the lower bound of estimation error. We use the vectors  $\boldsymbol{\kappa} = [\kappa_1, \kappa_2, \kappa_3]^T \triangleq [h, \omega, \varphi]^T$  and  $\hat{\boldsymbol{\kappa}} = [\hat{\kappa}_1, \hat{\kappa}_2, \hat{\kappa}_3]^T \triangleq [\hat{h}, \hat{\omega}, \hat{\varphi}]^T$  to represent the true values of unknown parameters and their estimated results. In particular,  $\hat{R} = 2c(\frac{\hat{\kappa}_2}{\alpha} + \tau')$  and  $R = 2c(\frac{\kappa_2}{\alpha} + \tau')$ . The covariance matrix of  $\boldsymbol{\kappa}$  is lower bounded by the inverse of Fisher information matrix (FIM)

$$\text{Cov}(\hat{\boldsymbol{\kappa}}) \geq \text{CRLB}(\boldsymbol{\kappa}) = \mathbf{I}^{-1}(\boldsymbol{\kappa}), \quad (35)$$

where  $[\mathbf{I}(\boldsymbol{\kappa})]_{ij} = -E\left(\frac{\partial^2 \log L}{\partial \kappa_i \partial \kappa_j}\right)$ . Here, the loglikelihood function  $\log L$  is given as

$$\log L \propto -\frac{1}{2} \int_0^T |\bar{y}(t) - \varrho(t)h \cos(\omega t + \varphi)|^2 dt. \quad (36)$$

The full expression of the FIM is derived in Appendix A for reader's reference. Moreover, we are interested in the estimation error of the target range,  $R$ . The following proposition provides an asymptotic expression of  $\text{CRLB}(R)$  for large  $\omega$ .

**Proposition 1.** *For large  $\omega$ , the CRLB of  $R$  is asymptotically*

$$\text{Var}(\hat{R}) \geq \text{CRLB}(R) \rightarrow \frac{8c^2 \bar{\varrho}_0}{\alpha^2 h^2 (\bar{\varrho}_0 \bar{\varrho}_2 - \bar{\varrho}_1^2)}, \quad (37)$$

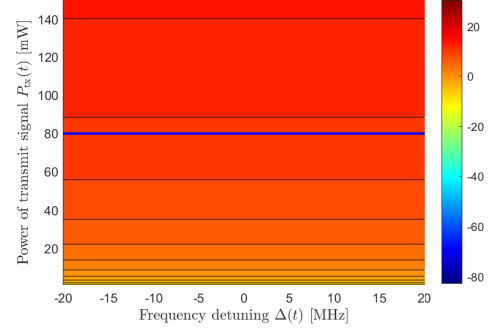
where  $\bar{\varrho}_0 \triangleq \int_0^T \varrho^2(t) dt$ ,  $\bar{\varrho}_1 \triangleq \int_0^T \varrho^2(t) t dt$ , and  $\bar{\varrho}_2 \triangleq \int_0^T \varrho^2(t) t^2 dt$ .

*Proof:* (See Appendix A).  $\square$

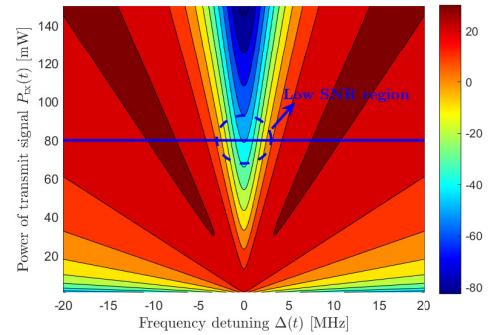
In Section VI numerical results will show that the target range estimated by the proposed algorithm could approach CRLB.

## V. SELF-HETERODYNE SENSING: SENSITIVITY MAXIMIZATION

In this section, we propose to maximize the RARE's sensitivity through the manipulation of the time-varying transmission power,  $P_{\text{tx}}(t)$ , which is also called *power-trajectory*



(a) Received SNR (dB) of a classical receiver.



(b) Received SNR (dB) of a RARE.

Figure 6. The effect of transmission power  $P_{\text{tx}}(t)$  and frequency detuning  $\Delta(t)$  on the received SNR for (a) a classical receiver and (b) a RARE. The maximum peak power and average power are  $P_{\text{pk}} = P_{\text{avg}} = 80$  mW.

(*P-trajectory*) design. Specifically, we first elaborate on the necessity of *P-trajectory* design for sensitivity maximization. Then, one heuristic *P-trajectory* is devised by investigating the asymptotically optimal transmission power under both off-resonant and near-resonant electron transition conditions. This design is subsequently extended to practical *P-trajectories* by incorporating the practical power constraints.

### A. Necessity of *P-trajectory* Design

From the signal model derived in (26), the sensing accuracy of RARE is largely affected by the time-varying amplitude  $\varrho(t)$ . A larger value of  $\varrho^2(t)$  can undoubtedly give rise to a higher SNR of RARE, defined as  $\text{SNR}(t) = \varrho^2(t)h^2$ , which thereby increases the sensing sensitivity. This observation motivates us to carefully regulate the trajectory of the time-varying transmission power,  $P_{\text{tx}}(t)$ , to maximize  $\varrho^2(t)$  and achieve the highest possible sensitivity of a RARE. From (26), the SNR is explicitly written as

$$\text{SNR}(t) = \underbrace{\frac{\mu_{34}^2 \Upsilon^2(\Omega_r(t), \Delta_r(t))}{\hbar^2 \Pi(\Omega_r(t), \Delta_r(t)) KB}}_{\text{Gain of RARE}} \underbrace{P_{\text{tx}}(t) G_{\text{tx}} h^2}_{\text{Received power}}. \quad (38)$$

One can observe from (38) that the transmission power,  $P_{\text{tx}}(t)$ , and the instantaneous frequency,  $\frac{d\vartheta_s(t)}{dt}$ , of the transmitted signal affect the received SNR in two aspects. First,  $P_{\text{tx}}(t)$  directly determines the power of the received sensing signal,



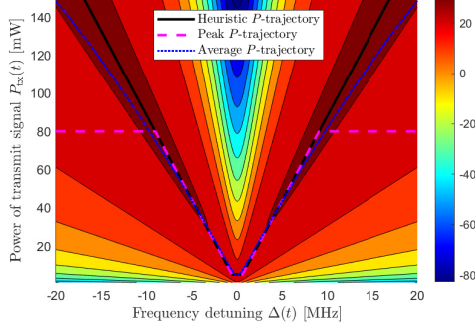


Figure 7. The designed heuristic and practical  $P$ -trajectories.

$P_{\text{tx}}(t)G_{\text{tx}}h^2$ . Second,  $P_{\text{tx}}(t)$  and  $\frac{d\vartheta_s(t)}{dt}$  influence the Rabi frequency,  $\Omega_r(t) = \frac{\mu_{34}}{\hbar}\sqrt{P_{\text{tx}}(t)G_{\text{tx}}'h'}$ , and frequency detuning,  $\Delta(t) = \frac{d\vartheta_s(t-\tau')}{dt} - \omega_{34}$ , of the reference signal, which further determine the gain of RARE. As a result, unlike the SNR of a classical receiver in (3) that is linearly dependent on the transmission power  $P_{\text{tx}}$ , the SNR of a RARE exhibits a complicated pattern with the transmission power,  $P_{\text{tx}}(t)$ .

We display the effect of transmission power and frequency detuning on the received SNR for a classical receiver and a RARE in Fig. 6(a) and Fig. 6(b), respectively. In the case of a classical receiver, as the frequency detuning of LFM waveform sweeps from  $-B/2$  to  $B/2$ , the received SNR remains unchanged when the transmission power is constant. Henceforth, a fixed transmission power is optimal for a classical receiver. However, as  $\Delta(t)$  sweeps from  $-B/2$  to  $B/2$ , a fixed transmission power may cause the RARE to encounter regions with extremely low SNRs. For example, if  $P_{\text{tx}}(t) \equiv 80$  mW, the RARE will experience a loss of over 50 dB in SNR as the frequency detuning increases from -10 MHz to 0 MHz. Thereafter, to reach the maximal sensitivity of self-heterodyne sensing, it is essential to have a time-varying  $P_{\text{tx}}(t)$  and carefully design the associated  $P$ -trajectory.

### B. Heuristic $P$ -trajectory Design

We first design a heuristic  $P$ -trajectory. As the SNR in (38) is a complicated function of  $P_{\text{tx}}(t)$  and  $\Delta(t)$ , it is difficult to find the optimal power  $P_{\text{tx}}^*(t)$  that maximizes the SNR for an arbitrary frequency detuning  $\Delta(t)$ . Fortunately, we are able to determine the optimal powers in certain special cases.

As depicted in Fig. 6(b), the highest SNR appears in the area (the dark red area) where both the frequency detuning and transmission power are large. We would like to capture this high SNR area at first. Specifically, recalling that  $\Omega_r(t) = \frac{\mu_{34}}{\hbar}\sqrt{P_{\text{tx}}(t)G_{\text{tx}}'h'}$ , we can replace the transmission power term,  $P_{\text{tx}}(t)$ , in (38) as  $P_{\text{tx}}(t) = \frac{\hbar^2}{\mu_{34}^2 h'^2 G_{\text{tx}}'} \Omega_r^2(t)$ . By further discarding the terms irrelevant to  $\Omega_r(t)$  and  $\Delta_r(t)$  in (38), it becomes convenient to show that

$$\text{SNR}(t) \propto \frac{\Upsilon^2(\Omega, \Delta)\Omega^2}{\Pi(\Omega, \Delta)} \Big|_{\Omega=\Omega_r(t), \Delta=\Delta_r(t)}. \quad (39)$$

Thereafter, maximizing the SNR is equivalent to maximizing the function  $|\Upsilon(\Omega, \Delta)\Omega|/\sqrt{\Pi(\Omega, \Delta)}$ . The following theorem

captures the highest  $|\Upsilon(\Omega, \Delta)\Omega|/\sqrt{\Pi(\Omega, \Delta)}$  when both the frequency detuning and transmission power are large.

**Theorem 1.** When  $\Omega \gg 1$  and  $|\Delta| \gg \Omega$ , the optimal  $\Omega^*$  that maximizes the SNR function  $\frac{|\Upsilon(\Omega, \Delta)\Omega|}{\sqrt{\Pi(\Omega, \Delta)}}$  is

$$\Omega^{*2} = k_1 |\Delta|, \quad (40)$$

where  $k_1 \triangleq \sqrt{\frac{C_3}{4C_1^2} \left( \sqrt{C_0^2 B_1^2 + 16C_1^2} - C_0 B_1 \right)}$ .

*Proof:* (See Appendix B).  $\square$

Leveraging Theorem 1 and the relationship  $P_{\text{tx}}(t) = \frac{\hbar^2}{\mu_{34}^2 h'^2 G_{\text{tx}}'} \Omega_r^2(t)$ , we can straightforwardly figure out that the optimal power that maximizes the SNR is

$$P_{\text{tx}}^*(t) = \frac{\hbar^2 k_1}{G_{\text{tx}}' h'^2 \mu_{34}^2} |\Delta(t)|. \quad (41)$$

According to (41), in the off-resonant case where  $|\Delta(t)|$  is large, the transmission power  $P_{\text{tx}}(t)$  should increase linearly with the absolute value of the frequency detuning,  $|\Delta(t)|$ .

Nevertheless, the optimality of (41) only holds for the off-resonant signal. In the case when the reference signal is nearly resonant ( $\Delta(t) \approx 0$ ) the transmission power computed by (41) would approach zero, which will shut down the sensing task and make SNR  $\approx 0$ . We provide the following theorem to circumvent this issue.

**Theorem 2.** When  $\Delta \rightarrow 0$ , the optimal  $\Omega^*$  that maximizes the SNR function  $\frac{|\Upsilon(\Omega, \Delta)\Omega|}{\sqrt{\Pi(\Omega, \Delta)}}$  is

$$\Omega^* = k_2 \triangleq \sqrt{\frac{C_2}{4C_1^2} \left( \sqrt{C_0^2 B_1^2 + 16C_1^2} - C_0 B_1 \right)}. \quad (42)$$

*Proof:* (See Appendix C).  $\square$

Similar to (41), the optimal transmission power for small  $|\Delta(t)|$  can be directly derived from Theorem 2 as

$$P_{\text{tx}}^*(t) = \frac{\hbar^2 k_2^2}{G_{\text{tx}}' h'^2 \mu_{34}^2}. \quad (43)$$

To summarize, while Theorem 1 captures the near-optimal transmission power for large detunings, Theorem 2 characterizes the near-optimal transmission power for small detunings. When  $\Delta(t) = \frac{k_2^2}{k_1}$ , the transmission powers calculated by (41) and (43) become equal. Leveraging these two theorems, the heuristic  $P$ -trajectory is designed as

$$P_{\text{tx}}(t) = \begin{cases} \frac{\hbar^2 k_2^2}{G_{\text{tx}}' h'^2 \mu_{34}^2} & \text{if } |\Delta(t)| \leq \frac{k_2^2}{k_1} \\ \frac{\hbar^2 k_1}{G_{\text{tx}}' h'^2 \mu_{34}^2} |\Delta(t)| & \text{if } \frac{k_2^2}{k_1} < |\Delta(t)| \leq \frac{B}{2} \end{cases}. \quad (44)$$

When the frequency detuning  $\Delta(t)$  of LFM waveform sweeps from  $-B/2$  to  $B/2$ , the transmission power  $P_{\text{tx}}(t)$  varies as (41) when  $k_2^2/k_1 < |\Delta(t)| \leq B/2$ , and is fixed as (43) when  $|\Delta(t)| \leq k_2^2/k_1$ . The designed heuristic  $P$ -trajectory is illustrated by the black line in Fig. 7. This trajectory can consistently achieve a high SNR for any frequency detuning.

### C. Practical $P$ -trajectory Design

Although the heuristic  $P$ -trajectory has already attained near-optimal sensitivity for a RARE, it does not consider

the practical transmission power constraints of a transmitter device. To address this issue, we further extend the heuristic  $P$ -trajectory to practical  $P$ -trajectories by considering both the peak-power constraint and the average-power constraint.

1) *Peak-power constrained  $P$ -trajectory (Peak  $P$ -trajectory)*: For devices with a limited peak power,  $P_{\text{pk}}$ , the transmission power  $P_{\text{tx}}(t)$  at any given time cannot exceed  $P_{\text{pk}}$ . To tackle this constraint, we truncate the power of the heuristic  $P$ -trajectory that surpasses  $P_{\text{pk}}$ . Specifically, when  $|\Delta(t)| = \Delta_{\text{pk}} \triangleq \frac{G'_{\text{tx}} h'^2 \mu_{34}^2 P_{\text{pk}}}{\hbar^2 k_1}$ , the power computed by (41) equals to  $P_{\text{pk}}$ . The peak  $P$ -trajectory is thus designed as

$$P_{\text{tx}}(t) = \begin{cases} \frac{\hbar^2 k_2^2}{G'_{\text{tx}} h'^2 \mu_{34}^2} & \text{if } |\Delta(t)| \leq \frac{k_2^2}{k_1} \\ \frac{\hbar^2 k_1}{G'_{\text{tx}} h'^2 \mu_{34}^2} |\Delta(t)| & \text{if } \frac{k_2^2}{k_1} < |\Delta(t)| \leq \Delta_{\text{pk}} \\ P_{\text{pk}} & \text{if } \Delta_{\text{pk}} < |\Delta(t)| \leq \frac{B}{2} \end{cases} \quad (45)$$

The designed  $P$ -trajectory is presented by the pink dotted line in Fig. 7. It always keeps the RARE in a high-SNR state.

2) *Average-power constrained  $P$ -trajectory (Average  $P$ -trajectory)*: To deal with devices with a average-power constraint, we adopt a numerical optimization method to refine the heuristic  $P$ -trajectory. Specifically, we first use discrete-time sequences to replace the previous continuous-time functions, such as  $P_{\text{tx}}(t)$  and  $\varrho(t)$ , for operational simplicity. Let the discrete time samples be  $t_s = \frac{s-1}{S}T$ ,  $s \in \{1, 2, \dots, S\}$ , where  $S$  is the number of samples. Then, the average-power constraint is formulated as

$$(C1) \quad \sum_{s=1}^S P_{\text{tx}}(t_s) \leq S P_{\text{avg}}, \quad (46)$$

where  $P_{\text{avg}}$  is the maximum average power. Moreover, we require the transmission power to be positive:

$$(C2) \quad P_{\text{tx}}(t_s) \geq 0, \quad \forall s. \quad (47)$$

Our objective is to maximize the average received SNR over all time samples, which can thus be formulated as

$$\max_{\{P_{\text{tx}}(t_s)\}_{s=1}^S} \frac{1}{S} \sum_{s=1}^S \varrho^2(t_s) \quad \text{s.t. (C1) \& (C2)}. \quad (48)$$

By solving (48), the designed average  $P$ -trajectory is able to meet the average power constraint while keeping the sensitivity of RARE high. As the objective function in (48) is nonconvex while the constraints (C1) and (C2) are convex, we can apply the primal-dual subgradient (PDS) method to solve (48) numerically [36]. The detailed PDS method is presented in Appendix E. Besides, the heuristic  $P$ -trajectory is regarded as the initial point to prevent a shallow local optimum.

The optimized average  $P$ -trajectory is plotted in the blue dotted line of Fig. 7. It slightly lowers down the power of the heuristic  $P$ -trajectory at the large detuning area. Nevertheless, the curve of the average  $P$ -trajectory is always located inside the dark red region with the highest SNRs, which gives rise to the near-optimal sensitivity of a RARE.

## VI. EXPERIMENTAL RESULTS

In this section, we present numerical experiments to verify the effectiveness of the proposed self-heterodyne approach.

Table I  
EXPERIMENTAL CONFIGURATIONS

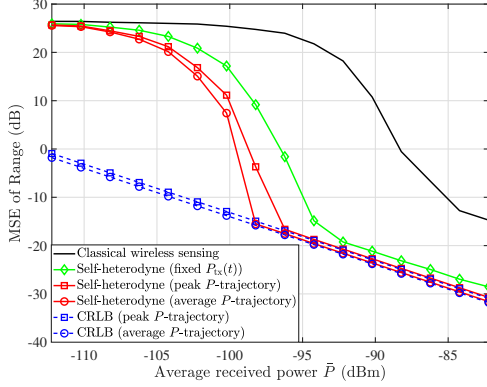
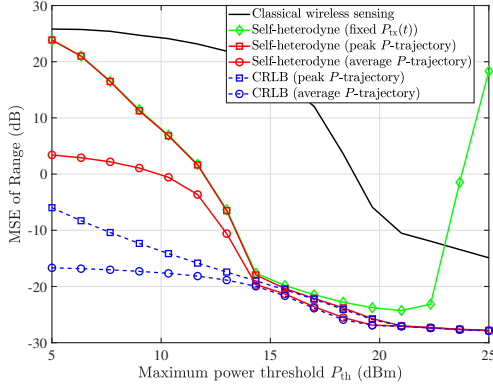
Parameters	Values
Energy levels, $\{ 1\rangle,  2\rangle\}$	$\{6S_{1/2}, 6P_{3/2}\}$
Energy levels, $\{ 3\rangle,  4\rangle\}$	$\{47D_{5/2}, 48P_{3/2}\}$
Transition dipole moment, $\mu_{34}$	$1.22 \times 10^{-26} \text{ C} \cdot \text{m}$
Transition dipole moment, $\mu_{12}$	$2.19 \times 10^{-29} \text{ C} \cdot \text{m}$
Decaying rates, $\gamma_2$	32.67 Mrad/s
Rabi frequencies, $\{\Omega_p, \Omega_c\}$	$\{36.2, 94.2\} \text{ Mrad/s}$
Wavelength of probe laser, $\lambda_p$	852 nm
Wavelength of coupling laser, $\lambda_c$	510 nm
Input power of probe laser, $P_{\text{in}}$	120 $\mu\text{W}$
Length of vapor cell, $L$	0.02 m
Density of atoms, $N_0$	$4.89 \times 10^{16} \text{ m}^{-3}$
Resistance, $R$	50 Ohm
Quantum efficiency, $\eta$	0.8
Circuits gains, $\{G_{\text{lna}}, G_{\text{rec}}\}$	$\{30, 0\} \text{ dB}$
Antenna gains, $\{G_{\text{tx}}, G'_{\text{tx}}, G_{\text{rx}}\}$	$\{6, -10, 6\} \text{ dBi}$
Equivalent noise temperature, $T_E$	100 K
Target range, $R$	$\mathcal{U}(1 \text{ m}, 1000 \text{ m})$
Cross-section, $\sigma_S$	10 dBsm
Frequencies, $\omega_{34}$ and $\omega_0$	$2\pi \times 6.95 \text{ GHz}$
Bandwidth, $B$	50 MHz
Symbol duration, $T$	100 $\mu\text{s}$
Transmitter-to-RARE delay, $\tau'$	1 ns
Transmitter-to-RARE fading, $h'^2$	-3 dB
Maximum power threshold, $P_{\text{th}}$	20 dBm

### A. Experimental Configurations

To account for a practical scenario, we follow the experimental configurations for the atoms and lasers in [20]. Otherwise specifically specified, the key parameters associated with their default values are given in Table I. The average received power of the sensing signal is defined as  $\bar{P} = \frac{1}{T} \int_0^T P_s(t) dt$ . The sensing performance is evaluated by the mean square error (MSE) in dB, which is defined as  $\text{MSE (dB)} = 10 \log_{10} \text{E}(|R - \hat{R}|^2)$ . Here, the unit of  $R$  and  $\hat{R}$  is meter. The target range  $R$  is randomly sampled from the uniform distribution  $\mathcal{U}(1 \text{ m}, 1000 \text{ m})$ . Besides, 3000 Monte-Carlo experiments are carried out to plot each figure. Six benchmarks are considered for comparison.

- *Classical wireless sensing*: The classical receiver is deployed for range sensing. The NLS method is used to recover the target range  $R$  from  $y_0(t)$  in (2).
- *Self-heterodyne (Fixed  $P_{\text{tx}}(t)$ )*: The proposed self-heterodyne based quantum wireless sensing scheme is adopted to estimate the target range. The transmitter power  $P_{\text{tx}}(t)$  is fixed as the power threshold,  $P_{\text{th}}$ .
- *Self-heterodyne (Peak  $P$ -trajectory)*: The designed peak  $P$ -trajectory is employed to enhance the sensitivity of self-heterodyne sensing.
- *Self-heterodyne (Average  $P$ -trajectory)*: The designed average  $P$ -trajectory is employed to enhance the sensitivity of self-heterodyne sensing.
- *CRLB (Peak  $P$ -trajectory)*: The CRLB in (37) with the peak  $P$ -trajectory is considered
- *CRLB (Average  $P$ -trajectory)*: The CRLB in (37) with the average  $P$ -trajectory is considered.

Note that the heterodyne-sensing described in Example 2 is not included into our experiment. This is because the considered

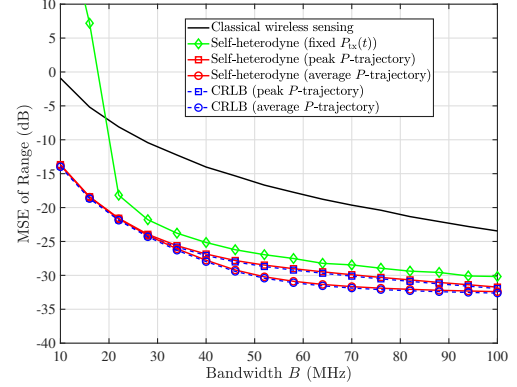
Figure 8. The effect of average received power  $\bar{P}$  on the MSE performance.Figure 9. MSE versus the maximum transmission power threshold  $P_{th}$ .

bandwidth,  $B = 50$  MHz, has significantly exceeded the typical instantaneous bandwidth of a RARE, 10 MHz. **At present, there exists no explainable model to accurately characterize the received signal or any algorithm capable of conducting range sensing within such heterodyne-sensing setups.**

### B. Experimental Results

To begin with, Fig. 8 illustrates the effect of the average received power  $\bar{P}$  on the MSE. Here, the variation of  $\bar{P}$  is caused by the different channel fadings,  $h'^2$ , at various target ranges,  $R$ . As the received power grows, the MSEs achieved by all compared benchmarks decline rapidly. In particular, the proposed self-heterodyne sensing schemes outperform the classical wireless sensing by 10~30 dB. This improvement is attributed to the extremely high sensitivity of a self-heterodyne RARE. Additionally, the designed  $P$ -trajectories can further reduce the MSE of a RARE by 1~15 dB, highlighting the effectiveness of the proposed  $P$ -trajectory. Moreover, the proposed self-heterodyne sensing algorithms can tightly approach their CRLBs when the received power  $\bar{P}$  is large.

The MSE performance as a function of the maximum transmission power threshold,  $P_{th}$ , is evaluated in Fig. 9. The power threshold ranges from 5 dBm to 25 dBm. It is evident from Fig. 9 that the proposed self-heterodyne sensing methods consume significantly less power than the classical sensing method for achieving a same level of MSE. For

Figure 10. MSE as a function of the system bandwidth  $B$ .

instance, to obtain a 0 dB MSE, the required transmission power is reduced from 18 dBm with a classical receiver to 10 dBm with a self-heterodyne RARE enhanced by the average  $P$ -trajectory. In addition, the MSE of the self-heterodyne sensing with a fixed power  $P_{tx}(t) = P_{th}$  gets exploded when  $P_{th} > 22$  dBm. The explosion is owing to the fact that the low SNR region imposed on the fixed  $P$ -trajectory becomes dominated when  $P_{th}$  increases, which can be seen in Fig. 6. Fortunately, the proposed average and peak  $P$ -trajectories can effectively circumvent these low SNR regions, enabling accurate range estimation across all considered transmission power thresholds  $P_{th}$ . Another finding of interest is that the average  $P$ -trajectory significantly outperforms the peak  $P$ -trajectory in the low transmit-power region. The reason is that a small value of  $P_{th}$  is far from the optimal transmission power  $\frac{h^2 k_1}{G'_{tx} h'^2 \mu_{34}^2} |\Delta(t)|$  for large detunings  $\Delta_r(t)$ , while it is close to the optimal transmission power  $\frac{h^2 k_2}{G'_{tx} h'^2 \mu_{34}^2}$  for large detunings  $\Delta_r(t)$ . In this context, the shape of the peak  $P$ -trajectory will be similar to that of a fixed  $P$ -trajectory without optimization, leading to a suboptimal performance. This insight states that an average power constrained device is more suitable for quantum wireless sensing under low transmission powers.

Finally, Fig. 10 assesses the influence of bandwidth,  $B$ , on the MSE of wireless sensing, with  $B$  ranging from 10 MHz to 100 MHz. Across all considered bandwidths, the self-heterodyne schemes can lower down the sensing MSE of the classical approach by 15 dB on average, demonstrating the wideband sensing ability of RARE. However, one can observe that the MSE of the classical wireless sensing declines more rapidly than that of the self-heterodyne sensing schemes, as the bandwidth increases. This trend is attributed to the fact that a larger bandwidth leads to a higher value of the detuning  $\Delta_r(t)$ , causing the reference signal to be far off-resonant from the transition frequency. Consequently, the gain and sensitivity of a RARE are remarkably diminished. Fortunately, this far off-resonant problem can be effectively addressed using various continuous-frequency sensing techniques, such as detecting off-resonant Stark shifts [14], [15] and broadening the transition frequency through the Zeeman effect [13]. The integration of these techniques with the proposed self-heterodyne sensing approach represents a crucial future direction to facilitate ultra-

broadband quantum wireless sensing.

## VII. CONCLUSIONS

We have proposed the self-heterodyne sensing approach to realize quantum wireless sensing without extra reference sources. It was discovered that a self-heterodyne RARE fundamentally operates as an atomic autocorrelator, enabling automatic conversion of the target range into the fluctuation frequency of the probe-laser power. Particularly, this autocorrelation mechanism allows a RARE to detect sensing signals with a wide bandwidth, paving the way for high-resolution quantum wireless sensing. Moreover, we have identified the critical role of  $P$ -trajectory in maximizing RARE sensitivity. Numerical results demonstrate that self-heterodyne sensing can reduce the MSE of range sensing by orders of magnitude.

This work represents a significant stride towards the development of next-generation quantum wireless sensing systems. We conclude by outlining potential avenues for future research. First, using self-heterodyne sensing to do multi-target detection remains an open problem. Furthermore, it is promising to extend self-heterodyne sensing to RARE-based Integrated Sensing and Communications (RARE-ISAC) systems. Last, while this work assumes fixed Rabi frequencies and zero frequency detunings for the probe and coupling lasers, dynamically optimizing these time-varying parameters could further enhance RARE sensitivity.

## APPENDIX

### A. Expression of FIM and Proof of Proposition 1

Each element of the FIM is calculated as

$$\begin{cases} -E\left(\frac{\partial^2 \log L}{\partial h^2}\right) = \int_0^T \varrho^2(t) \cos^2(\omega t + \varphi) dt \\ -E\left(\frac{\partial^2 \log L}{\partial \omega^2}\right) = h^2 \int_0^T \varrho^2(t) t^2 \sin^2(\omega t + \varphi) dt \\ -E\left(\frac{\partial^2 \log L}{\partial \varphi^2}\right) = h^2 \int_0^T \varrho^2(t) \sin^2(\omega t + \varphi) dt \\ -E\left(\frac{\partial^2 \log L}{\partial \omega \partial \varphi}\right) = h^2 \int_0^T \varrho^2(t) t \sin^2(\omega t + \varphi) dt \\ -E\left(\frac{\partial^2 \log L}{\partial \omega \partial \varphi}\right) = -\frac{h}{2} \int_0^T \varrho^2(t) \sin(2\omega t + 2\varphi) dt \\ -E\left(\frac{\partial^2 \log L}{\partial h \partial \omega}\right) = -\frac{h}{2} \int_0^T \varrho^2(t) t \sin(2\omega t + 2\varphi) dt \end{cases} \quad (49)$$

For large  $\omega$ , the functions  $\cos(2\omega t + 2\varphi)$  and  $\sin(2\omega t + 2\varphi)$  will fluctuate much faster than  $\varrho^2(t)$ ,  $\varrho^2(t)t$ , and  $\varrho^2(t)t^2$ . In this context, the integration between a former one and a latter one will gradually average to zero. Therefore, the elements of FIM in (49) are asymptotically

$$\begin{cases} -E\left(\frac{\partial^2 \log L}{\partial h^2}\right) \rightarrow \frac{1}{2} \int_0^T \varrho^2(t) dt \\ -E\left(\frac{\partial^2 \log L}{\partial \omega^2}\right) \rightarrow \frac{h^2}{2} \int_0^T \varrho^2(t) t^2 dt \\ -E\left(\frac{\partial^2 \log L}{\partial \varphi^2}\right) \rightarrow \frac{h^2}{2} \int_0^T \varrho^2(t) dt \\ -E\left(\frac{\partial^2 \log L}{\partial \omega \partial \varphi}\right) \rightarrow \frac{h^2}{2} \int_0^T \varrho^2(t) t dt \\ -E\left(\frac{\partial^2 \log L}{\partial h \partial \omega}\right), -E\left(\frac{\partial^2 \log L}{\partial h \partial \varphi}\right) \rightarrow 0 \end{cases} \quad (50)$$

We define the notations  $\bar{\varrho}_0 \triangleq \int_0^T \varrho^2(t) dt$ ,  $\bar{\varrho}_1 \triangleq \int_0^T \varrho^2(t) t dt$ , and  $\bar{\varrho}_2 \triangleq \int_0^T \varrho^2(t) t^2 dt$ . The inverse of FIM is thus

$$\mathbf{I}^{-1}(\boldsymbol{\kappa}) = \begin{pmatrix} \frac{2}{\bar{\varrho}_0} & 0 & 0 \\ 0 & \frac{2\bar{\varrho}_0}{h^2(\bar{\varrho}_2\bar{\varrho}_0 - \bar{\varrho}_1^2)} & \frac{-2\bar{\varrho}_1}{h^2(\bar{\varrho}_2\bar{\varrho}_0 - \bar{\varrho}_1^2)} \\ 0 & \frac{-2\bar{\varrho}_1}{h^2(\bar{\varrho}_2\bar{\varrho}_0 - \bar{\varrho}_1^2)} & \frac{2\bar{\varrho}_2}{h^2(\bar{\varrho}_2\bar{\varrho}_0 - \bar{\varrho}_1^2)} \end{pmatrix}. \quad (51)$$

As a result, the CRLB of the frequency parameter  $\omega$  is

$$\text{CRLB}(\omega) = \frac{2\bar{\varrho}_0}{h^2(\bar{\varrho}_2\bar{\varrho}_0 - \bar{\varrho}_1^2)}. \quad (52)$$

The associated CRLB of target range  $R = 2c(\frac{\omega}{\alpha} + \tau')$  is

$$\text{CRLB}(R) = \frac{8c^2\bar{\varrho}_0}{\alpha^2 h^2(\bar{\varrho}_2\bar{\varrho}_0 - \bar{\varrho}_1^2)}. \quad (53)$$

### B. Proof of Theorem 1

The explicit expression of  $\frac{\Upsilon(\Omega, \Delta)\Omega}{\sqrt{\Pi(\Omega, \Delta)}}$  is written as

$$\begin{aligned} \frac{|\Upsilon(\Omega, \Delta)\Omega|}{\sqrt{\Pi(\Omega, \Delta)}} &= 2\sqrt{P_{\text{in}}}C_0B_1 \frac{\Omega^4(C_2\Omega^2 + 2C_3\Delta^2)}{(C_1\Omega^4 + C_2\Omega^2 + C_3\Delta^2)^2} \\ &\times \exp\left\{-\frac{\frac{1}{2}C_0B_1\Omega^4}{C_1\Omega^4 + C_2\Omega^2 + C_3\Delta^2}\right\}. \end{aligned} \quad (54)$$

When  $\Delta \gg \Omega$  and  $\Omega \gg 0$ , we have  $C_3\Delta^2 \gg C_2\Omega^2$  and  $C_1\Omega^4 \gg C_2\Omega^2$ . In this way, we can safely remove the term  $C_2\Omega^2$  in (54) and rewrite  $\frac{\Upsilon(\Omega, \Delta)\Omega}{\sqrt{\Pi(\Omega, \Delta)}}$  as

$$\begin{aligned} \frac{|\Upsilon(\Omega, \Delta)\Omega|}{\sqrt{\Pi(\Omega, \Delta)}} &\propto e^{-\frac{\frac{1}{2}C_0B_1\Omega^4}{C_1\Omega^4 + C_3\Delta^2}} \frac{2C_3\Omega^4\Delta^2}{(C_1\Omega^4 + C_3\Delta^2)^2} \\ &= e^{-\frac{\frac{1}{2}C_0B_1\frac{\Omega^4}{\Delta^2}}{C_1\frac{\Omega^4}{\Delta^2} + C_3}} \frac{2C_3\frac{\Omega^4}{\Delta^2}}{(C_1\frac{\Omega^4}{\Delta^2} + C_3)^2} \triangleq \xi\left(\frac{\Omega^4}{\Delta^2}\right). \end{aligned} \quad (55)$$

Thereafter, maximizing  $\frac{|\Upsilon(\Omega, \Delta)\Omega|}{\sqrt{\Pi(\Omega, \Delta)}}$  is equivalent to maximizing  $\xi\left(\frac{\Omega^4}{\Delta^2}\right)$ . Specifically, the derivative of  $\xi(x)$  is

$$\frac{d\xi(x)}{dx} = 2C_3e^{-\frac{\frac{1}{2}C_0B_1x}{C_1x + C_3}} \frac{C_3^2 - \frac{1}{2}C_0C_3B_1x - C_1^2x^2}{(C_1x + C_3)^4}. \quad (56)$$

After some tedious calculations, the maximum of  $\xi(x)$  is achieved when

$$x^* = \frac{C_3}{4C_1^2} \left( \sqrt{C_0^2B_1^2 + 16C_1^2} - C_0B_1 \right). \quad (57)$$

By invoking the relationship  $\frac{\Omega^{*4}}{\Delta^{*2}} = x^*$ , we obtain Theorem 1.

### C. Proof of Theorem 2

When  $\Delta \rightarrow 0$ , we can safely remove the term  $C_3\Delta^2$  in  $\frac{|\Upsilon(\Omega, \Delta)\Omega|}{\sqrt{\Pi(\Omega, \Delta)}}$  and simplify it as

$$\frac{|\Upsilon(\Omega, \Delta)\Omega|}{\sqrt{\Pi(\Omega, \Delta)}} \propto e^{-\frac{\frac{1}{2}C_0B_1\Omega^2}{C_1\Omega^2 + C_2}} \frac{C_2\Omega^2}{(C_1\Omega^2 + C_2)^2} \triangleq \zeta(\Omega^2). \quad (58)$$

Thereafter, maximizing  $\frac{|\Upsilon(\Omega, \Delta)\Omega|}{\sqrt{\Pi(\Omega, \Delta)}}$  is equivalent to maximizing  $\zeta(\Omega^2)$ . Moreover, by comparing the equations (55) and (58), one can figure out that the only difference between the functions  $\xi(x)$  and  $\zeta(x)$  is that the coefficient  $C_3$  in  $\xi(x)$  is changed as  $C_2$  in  $\zeta(x)$ . Therefore, the optimal  $x^*$  that maximizes  $\zeta(x)$  is clearly

$$x^* = \frac{C_2}{4C_1^2} \left( \sqrt{C_0^2B_1^2 + 16C_1^2} - C_0B_1 \right). \quad (59)$$

By invoking the relationship  $\Omega^{*2} = x^*$ , we obtain Theorem 2.



### D. The PDS method for solving (48)

We consider to solve (48) using the PDS method [36]. Firstly, we introduce the Lagrange multipliers  $\boldsymbol{\nu} = [\nu_1, \dots, \nu_S]^T$  and  $v$  as well as a positive super-parameter  $\beta > 0$ . We further define the optimization variable as  $\mathbf{p} = [P_{tx}(t_1), \dots, P_{tx}(t_S)]^T$ . The augmented Lagrangian function of (48) can be written as

$$\mathcal{L} = g(\mathbf{p}) + v f(\mathbf{p}) + \boldsymbol{\nu}^T \mathbf{h}(\mathbf{p}) + \beta(f^2(\mathbf{p}) + \|\mathbf{h}(\mathbf{p})\|^2), \quad (60)$$

where functions  $g(\mathbf{p})$ ,  $f(\mathbf{p})$ , and  $\mathbf{h}(\mathbf{p})$  are defined as  $g(\mathbf{p}) \triangleq -\frac{1}{S} \sum_{s=1}^S \varrho^2(t_s)$ ,  $f(\mathbf{p}) \triangleq \left( \sum_{s=1}^S P_{tx}(t_s) - SP_{avg} \right)^+$ , and  $\mathbf{h}(\mathbf{p}) \triangleq [(-P_{tx}(t_1))^+, \dots, (-P_{tx}(t_S))^+]^T$ . Next, we introduce a superscript  $i$  to each variable as the iteration index, and the iterative formulas of  $\mathbf{p}^i$ ,  $\boldsymbol{\mu}^i$ , and  $v^i$  are written as

$$\begin{pmatrix} \mathbf{p}^{i+1} \\ v^{i+1} \\ \boldsymbol{\nu}^{i+1} \end{pmatrix} = \begin{pmatrix} \mathbf{p}^i \\ v^i \\ \boldsymbol{\nu}^i \end{pmatrix} - \varpi^i \begin{pmatrix} \partial \mathcal{L} / \partial \mathbf{p} |_{\mathbf{p}=\mathbf{p}^i} \\ -\partial \mathcal{L} / \partial v |_{v=v^i} \\ -\partial \mathcal{L} / \partial \boldsymbol{\nu} |_{\boldsymbol{\nu}=\boldsymbol{\nu}^i} \end{pmatrix}, \quad (61)$$

where the step length  $\varpi^i > 0$  is a sufficiently small value. By simultaneously optimizing  $\mathbf{p}$ ,  $\boldsymbol{\mu}$ , and  $v$  until convergence, the  $P$ -trajectory can be finally obtained.

### REFERENCES

- [1] B. Liu, L. Zhang, Z. Liu, Z. Deng, D. Ding, B. Shi, and G. Guo, "Electric field measurement and application based on Rydberg atoms," *Electromagn. Sci.*, vol. 1, no. 2, pp. 1–16, Jun. 2023.
- [2] M. Cui, Q. Zeng, and K. Huang, "Rydberg atomic receiver: Next frontier of wireless communications," *arXiv preprint arXiv:2412.12485*, Dec. 2024.
- [3] C. T. Fancher, D. R. Scherer, M. C. S. John, and B. L. S. Marlow, "Rydberg atom electric field sensors for communications and sensing," *IEEE Trans. Quantum Eng.*, vol. 2, no. 3501313, pp. 1–13, Mar. 2021.
- [4] M. Cui, Q. Zeng, and K. Huang, "Towards atomic MIMO receivers," *IEEE J. Sel. Areas Commun.*, vol. 43, no. 3, pp. 659–673, 2025.
- [5] Y. Chen, X. Guo, C. Yuen, Y. Zhao, Y. Guan, C. M. S. See, M. Debbah, and L. Hanzo, "Harnessing Rydberg atomic receivers: From quantum physics to wireless communications," *arXiv preprint arXiv:2501.11842*, Jan. 2025.
- [6] H. Zhang, Y. Ma, K. Liao, W. Yang, Z. Liu, D. Ding, H. Yan, W. Li, and L. Zhang, "Rydberg atom electric field sensing for metrology, communication and hybrid quantum systems," *Sci. Bull.*, vol. 69, no. 10, pp. 1515–1535, May 2024.
- [7] F. Zhang, B. Jin, Z. Lan, Z. Chang, D. Zhang, Y. Jiao, M. Shi, and J. Xiong, "Quantum wireless sensing: Principle, design and implementation," in *Proc. Annu. Int. Conf. Mobile Comput. Netw. (ACM MobiCom'23)*, Oct. 2023, pp. 1–15.
- [8] S. S. A. Yuan, X. Y. I. Xu, J. Yuan, G. Xie, C. Huang, X. Chen, Z. Huang, and W. E. I. Sha, "Electromagnetic modeling and capacity analysis of Rydberg atom-based MIMO system," *IEEE Antennas Wireless Propag. Lett.*, pp. 1–5, 2025.
- [9] M. Cai, S. You, S. Zhang, Z. Xu, and H. Liu, "Sensitivity extension of atom-based amplitude-modulation microwave electrometry via high Rydberg states," *Appl. Phys. Lett.*, vol. 122, no. 16, p. 161103, Apr. 2023.
- [10] H. Fan, S. Kumar, J. Sedlacek, H. Kübler, S. Karimkashi, and J. P. Shaffer, "Atom based RF electric field sensing," *J. Phys. B: At. Mol. Opt. Phys.*, vol. 48, no. 20, p. 202001, Sep. 2015.
- [11] G. Sandidge, G. Santamaria-Botello, E. Bottomley, H. Fan, and Z. Popović, "Resonant structures for sensitivity enhancement of Rydberg-atom microwave receivers," *IEEE Trans. Microw. Theory Techn.*, vol. 72, no. 4, pp. 2057–2066, Apr. 2024.
- [12] D. H. Meyer, J. C. Hill, P. D. Kunz, and K. C. Cox, "Simultaneous multiband demodulation using a Rydberg atomic sensor," *Phys. Rev. Appl.*, vol. 19, p. 014025, Jan. 2023.
- [13] Y. Shi, C. Li, K. Ouyang, W. Ren, W. Li, M. Cao, Z. Xue, and M. Shi, "Tunable frequency of a microwave mixed receiver based on Rydberg atoms under the Zeeman effect," *Opt. Exp.*, vol. 31, no. 22, pp. 36 255–36 262, Oct. 2023.
- [14] J. Hu, H. Li, R. Song, J. Bai, Y. Jiao, J. Zhao, and S. Jia, "Continuously tunable radio frequency electrometry with Rydberg atoms," *Appl. Phys. Lett.*, vol. 121, p. 014002, Jul. 2022.
- [15] Z. Song, H. Liu, X. Liu, W. Zhang, H. Zou, J. Zhang, and J. Qu, "Rydberg-atom-based digital communication using a continuously tunable radio-frequency carrier," *Opt. Exp.*, vol. 27, no. 6, pp. 8848–8857, Mar 2019.
- [16] D. H. Meyer, K. C. Cox, F. K. Fatemi, and P. D. Kunz, "Digital communication with Rydberg atoms and amplitude-modulated microwave fields," *Appl. Phys. Lett.*, vol. 112, no. 21, p. 211108, May 2018.
- [17] D. A. Anderson, R. E. Sapiro, and G. Raithel, "An atomic receiver for AM and FM radio communication," *IEEE Trans. Antennas Propag.*, vol. 69, no. 5, pp. 2455–2462, May 2021.
- [18] Z. Jia, Q. Li, Y. Wang, Y. You, B. Chen, and Y. Peng, "Properties and utilization in time-dependent Rydberg EIT," *Opt. Continuum*, vol. 3, no. 2, p. 135, Feb. 2024.
- [19] M. T. Simons, A. H. Haddab, J. A. Gordon, and C. L. Holloway, "A Rydberg atom-based mixer: Measuring the phase of a radio frequency wave," *Appl. Phys. Lett.*, vol. 114, no. 11, p. 114101, Mar. 2019.
- [20] M. Jing, Y. H. Hu, J. Ma, H. Zhang, L. Zhang, L. Xiao, and S. Jia, "Atomic superheterodyne receiver based on microwave-dressed Rydberg spectroscopy," *Nat. Phys.*, vol. 1, pp. 911–915, Jun. 2020.
- [21] G. Gao, M. Chen, H. Feng, Z. Zhu, A. Chen, Z. Wu, T. Mao, W. Dai, P. Peng, and D. Zheng, "Rydberg communication antennas with self-decoupling for dynamic radar interference based on heterodyne technology," *Appl. Phys. Lett.*, vol. 126, no. 13, p. 134002, Apr. 2025.
- [22] A. K. Robinson, N. Prajapati, D. Senic, M. T. Simons, and C. L. Holloway, "Determining the angle-of-arrival of a radio-frequency source with a Rydberg atom-based sensor," *Appl. Phys. Lett.*, vol. 118, no. 11, p. 114001, Mar. 2021.
- [23] B. Xu, J. Zhang, Z. Chen, B. Cheng, Z. Liu, Y.-C. Wu, and B. Ai, "Channel estimation for Rydberg atomic receivers," *arXiv preprint arXiv:2503.08985*, Mar. 2025.
- [24] H. Kim, H. Park, and S. Kim, "Quantum-MUSIC: Multiple signal classification for quantum wireless sensing," *IEEE Wireless Commun. Lett.*, 2025.
- [25] T. Gong, C. Yuen, C. M. S. See, M. Debbah, and L. Hanzo, "Rydberg atomic quantum receivers for multi-target DOA estimation," *arXiv preprint arXiv:2501.02820*, Jan. 2025.
- [26] G. Jones and B. Boashash, "Instantaneous frequency, instantaneous bandwidth and the analysis of multicomponent signals," in *Proc. International Conference on Acoustics, Speech, and Signal Processing*, 1990, pp. 2467–2470.
- [27] B. Yang, Y. Yan, X. Li, L. Xiao, X. Li, L. Chen, J. Deng, and H. Cheng, "Highly sensitive microwave electrometry with enhanced instantaneous bandwidth," *Phys. Rev. Appl.*, vol. 21, no. 3, p. L031003, Mar. 2024.
- [28] M. I. Skolnik, *Radar Handbook*, 3rd. New York: McGraw-Hill, 2004.
- [29] M. Malanowski, K. Kulpa, J. Kulpa, P. Samczynski, and J. Misiurewicz, "Analysis of detection range of FM-based passive radar," *IET Radar, Sonar & Navigation*, vol. 8, no. 2, pp. 153–159, 2014.
- [30] B. Boashash, "Estimating and interpreting the instantaneous frequency of a signal. II. Algorithms and applications," *Proc. IEEE*, vol. 80, no. 4, pp. 540–568, Apr. 1992.
- [31] S. Nandi and D. Kundu, "Asymptotic properties of the least squares estimators of the parameters of the chirp signals," *Ann. Inst. Stat. Math.*, vol. 56, no. 3, pp. 529–544, Sep. 2004.
- [32] S. Wu, C. Gong, and R. Ni, "Atomic superheterodyne receiver sensitivity estimation based on homodyne readout," *arXiv preprint arXiv:2309.16097*, Sep. 2023.
- [33] A. Ksiezzyk, M. Plotka, K. Abratkiewicz, R. Maksymiuk, J. Wszolek, P. Samczyński, and T. P. Zieliński, "Opportunities and limitations in radar sensing based on 5G broadband cellular networks," *IEEE Aerosp. Electron. Syst. Mag.*, vol. 38, no. 9, pp. 4–21, Sep. 2023.
- [34] B. N. Miller, D. H. Meyer, T. Virtanen, C. M. O'Brien, and K. C. Cox, "RydQuLe: A graph-based paradigm for modeling Rydberg and atomic sensors," *Comput. Phys. Commun.*, vol. 294, p. 108952, Jan. 2024.
- [35] B. Boashash, "Estimating and interpreting the instantaneous frequency of a signal. I. Fundamentals," *Proc. IEEE*, vol. 80, no. 4, pp. 520–538, Apr. 1992.
- [36] Y. Nesterov, "Primal-dual subgradient methods for convex problems," *Math. Program.*, vol. 120, no. 1, pp. 221–259, Aug. 2009.